



NAVAL POSTGRADUATE SCHOOL

MONTEREY, CALIFORNIA

THESIS

POINT DEFECT PROPERTIES IN IRON CHROMIUM ALLOYS

by

Harun Dogo

September 2006

Thesis Advisor:
Second Reader:

Craig Smith
Xavier Maruyama

Approved for public release; distribution is unlimited

THIS PAGE INTENTIONALLY LEFT BLANK

REPORT DOCUMENTATION PAGE			<i>Form Approved OMB No. 0704-0188</i>	
Public reporting burden for this collection of information is estimated to average 1 hour per response, including the time for reviewing instruction, searching existing data sources, gathering and maintaining the data needed, and completing and reviewing the collection of information. Send comments regarding this burden estimate or any other aspect of this collection of information, including suggestions for reducing this burden, to Washington headquarters Services, Directorate for Information Operations and Reports, 1215 Jefferson Davis Highway, Suite 1204, Arlington, VA 22202-4302, and to the Office of Management and Budget, Paperwork Reduction Project (0704-0188) Washington DC 20503.				
1. AGENCY USE ONLY (Leave blank)		2. REPORT DATE September 2006	3. REPORT TYPE AND DATES COVERED Master's Thesis	
4. TITLE AND SUBTITLE Point Defect Properties in Iron Chromium Alloys			5. FUNDING NUMBERS	
6. AUTHOR(S) Harun Dogo				
7. PERFORMING ORGANIZATION NAME(S) AND ADDRESS(ES) Naval Postgraduate School Monterey, CA 93943-5000			8. PERFORMING ORGANIZATION REPORT NUMBER	
9. SPONSORING /MONITORING AGENCY NAME(S) AND ADDRESS(ES) Department of Energy, University of California, Lawrence Livermore National Laboratory, 7000 East Avenue, Livermore, CA 94550			10. SPONSORING/MONITORING AGENCY REPORT NUMBER W-7405-Eng-48	
11. SUPPLEMENTARY NOTES The views expressed in this thesis are those of the author and do not reflect the official policy or position of the Department of Defense or the U.S. Government.				
12a. DISTRIBUTION / AVAILABILITY STATEMENT Approved for public release; distribution is unlimited			12b. DISTRIBUTION CODE A	
13. ABSTRACT (maximum 200 words) <p>The behavior of Fe-Cr alloys under irradiation is in part controlled by the characteristics of point defects generated by high energy collision. Radiation enhanced diffusion and radiation induced precipitation are among the mechanisms that lead to changes in the microstructure under irradiation, and are thus controlling effects such as swelling and α' precipitation. Point defects in Fe-Cr alloys are diverse in nature due to their interaction with a variety of local solute configurations. <i>Ab initio</i> results indicate that the magnetic structure of the alloy is critical in determining its energetics. The ability to model these properties with classic potentials is still to be proven. In this work a detailed comparison between <i>ab initio</i> and classic values of a variety of point defects configurations is performed, testing in this way the extent to which classic potentials can be reliably used for radiation damage studies, and evaluating the dependence of point defect formation energies on Cr concentration.</p>				
14. SUBJECT TERMS Radiation damage, alloy, iron, chromium, steel, Fe-Cr, point defect, fast nuclear reactor, Generation IV, nuclear materials			15. NUMBER OF PAGES 77	
			16. PRICE CODE	
17. SECURITY CLASSIFICATION OF REPORT Unclassified	18. SECURITY CLASSIFICATION OF THIS PAGE Unclassified	19. SECURITY CLASSIFICATION OF ABSTRACT Unclassified	20. LIMITATION OF ABSTRACT UL	

NSN 7540-01-280-5500

Standard Form 298 (Rev. 2-89)
Prescribed by ANSI Std. Z39-18

THIS PAGE INTENTIONALLY LEFT BLANK

Approved for public release; distribution is unlimited

POINT DEFECT PROPERTIES IN IRON-CHROMIUM ALLOYS

Harun Dogo
Lieutenant, Armed Forces of Bosnia and Herzegovina
B.S., United States Air Force Academy, 2003

Submitted in partial fulfillment of the
requirements for the degree of

MASTER OF SCIENCE IN APPLIED PHYSICS

from the

**NAVAL POSTGRADUATE SCHOOL
September 2006**

Author: Harun Dogo

Approved by: Dr. Craig F. Smith
Thesis Advisor

Dr. Xavier K. Maruyama
Second Reader/Co-Advisor

Dr. James H. Luscombe
Chairman, Department of Physics

THIS PAGE INTENTIONALLY LEFT BLANK

ABSTRACT

The behavior of Fe-Cr alloys under irradiation is in part controlled by the characteristics of point defects generated by high energy collision. Radiation enhanced diffusion and radiation induced precipitation are among the mechanisms that lead to changes in the microstructure under irradiation, and are thus controlling effects such as swelling and α' precipitation. Point defects in Fe-Cr alloys are diverse in nature due to their interaction with a variety of local solute configurations. *Ab initio* results indicate that the magnetic structure of the alloy is critical in determining its energetics. The ability to model these properties with classic potentials is still to be proven. In this work a detailed comparison between *ab initio* and classic values of a variety of point defects configurations is performed, testing in this way the extent to which classic potentials can be reliably used for radiation damage studies, and evaluating the dependence of point defect formation energies on Cr concentration.

THIS PAGE INTENTIONALLY LEFT BLANK

TABLE OF CONTENTS

I.	INTRODUCTION.....	1
II.	BACKGROUND	3
	A. HISTORY OF NUCLEAR POWER.....	3
	B. FUTURE DIRECTIONS IN NUCLEAR POWER	6
	C. FAST SPECTRUM NUCLEAR REACTOR DESIGN FEATURES	9
	D. SSTAR PROGRAM OVERVIEW	11
III.	MOTIVATION	13
	A. RADIATION DAMAGE	13
	B. MACRO-LEVEL EFFECTS OF RADIATION DAMAGE	16
	C. MATERIAL ISSUES FOR GENERATION IV NUCLEAR ENERGY SYSTEMS.....	18
	D. MULTI-SCALE APPROACH TO MATERIAL SCIENCE MODELING.....	20
IV.	THEORY AND METHODOLOGY FOR COMPUTATION	23
	A. INTRODUCTION.....	23
	B. THE MANY-BODY POTENTIAL	24
	C. THE FREE ENERGY EXPRESSION.....	25
	D. THE CROSS PAIR POTENTIAL	27
	E. THE MOLECULAR DYNAMICS CODE	28
V.	PROCEDURE AND RESULTS	31
	A. RESEARCH PLAN	31
	B. CHARACTERIZING THE PERFORMANCE OF THE CODE: THE STUDY OF DEFECTS IN PURE ELEMENTS	32
	C. EVALUATING THE VACANCY ENERGY OF FORMATION.....	36
	D. OBTAINING THE FORMATION ENERGIES OF INTERSTITIALS ..	38
VI.	ANALYSIS AND CONCLUSION.....	43
	A. VACANCIES.....	43
	B. SELF-INTERSTITIALS	46
	C. MIXED INTERSTITIALS.....	47
	D. CONCLUSIONS	52
VII.	SUMMARY OF RESEARCH	55
	LIST OF REFERENCES.....	57
	INITIAL DISTRIBUTION LIST	61

THIS PAGE INTENTIONALLY LEFT BLANK

LIST OF FIGURES

Figure 1.	Chicago Pile 1 Reaches Criticality [3].	3
Figure 2.	Neutron Cross-Sections for Fission of Uranium and Plutonium [4].	4
Figure 3.	A Moderated Chain Reaction.	5
Figure 4.	Overview of differences between fast and thermal absorption processes.	8
Figure 5.	Overview of Reactor Technology Development [10].	9
Figure 6.	Lead-Cooled Fast Reactor Diagram [10].	10
Figure 7.	Diagram of a Potential SSTAR Design [14].	11
Figure 8.	SSTAR Deployment [13].	12
Figure 9.	Vacancy Site in a Crystalline Structure [16].	13
Figure 10.	Interstitial Atom in a Crystal Lattice [16].	14
Figure 11.	$\langle 100 \rangle$ Interstitial [17].	14
Figure 12.	$\langle 110 \rangle$ Interstitial [17].	15
Figure 13.	$\langle 111 \rangle$ Interstitial [17].	15
Figure 14.	Radiation Induced Swelling [21].	17
Figure 15.	Irradiation Creep of Nuclear Fuel Pin Cladding [23].	17
Figure 16.	Diagram of Material Hardening and Embrittlement Evolution [18].	18
Figure 17.	Temporal and Spatial Placement of Phenomena [27].	21
Figure 18.	Global View of Multi-scale Material Modeling Effort [28].	22
Figure 19.	Ab Initio Calculations of Fe-Cr mixing enthalpy [35].	25
Figure 20.	Formation Energy of the Alloy as Predicted by the Potential Used in This Work [29].	25
Figure 21.	Heat of Formation Fit Below 6% Cr concentration.	35
Figure 22.	Polynomial fit in the sub 6% Cr concentration region.	40
Figure 23.	Polynomial fit to the 6-20 % region of Cr concentration.	40
Figure 24.	Vacancy Formation Energies in Iron.	44
Figure 25.	Vacancy Formation Energies in Chromium.	44
Figure 26.	Linear Interpolation Between EFV in Fe and Cr.	45
Figure 27.	Evolution of Vacancy Formation Energy as a Function of Cr.	45
Figure 28.	Formation Energies for Self-Interstitials in Iron [45].	47
Figure 29.	Formation Energies for Self-Interstitials in Chromium.	48
Figure 30.	Energy Histogram for Self-Interstitial Samples in the $\langle 110 \rangle$ direction at higher Cr Concentration.	48
Figure 31.	Histogram of Energies for Self-Interstitial Samples in the $\langle 110 \rangle$ direction at lower Cr Concentration.	49
Figure 32.	Histogram of Energies for Self-Interstitial Samples in $\langle 111 \rangle$.	49
Figure 33.	Evolution Self-Interstitial Formation Energies	50
Figure 34.	Partition Function for Stability of Self –Interstitial in $\langle 111 \rangle$.	50
Figure 35.	Evolution of Mixed-Interstitial Formation Energies.	51
Figure 36.	Combined Interstitial Evolution Plot.	51
Figure 37.	Research methodology [29].	55
Figure 38.	Development of the stability function for Fe self-interstitial in $\langle 110 \rangle$.	56

THIS PAGE INTENTIONALLY LEFT BLANK

LIST OF TABLES

Table 1.	Operating Conditions for Advanced Nuclear Applications [25]	19
Table 2.	Chemical Composition of Potential Generation IV Structural Materials [26].	19
Table 3.	Values of the Redlich-Kister expansion coefficients for Eq. (6)	27
Table 4.	4 th Order Polynomial Coefficient for $h(x)$, as obtained by minimization.	28
Table 5.	Table of Final Values of Total Enthalpy for Pure Element Samples.....	33
Table 6.	Values of $\Delta h[\text{eV/atom}]$ as obtained by modeling.	35
Table 7.	Formation Energies for the Pure Element Characterization.	36
Table 8.	Total Enthalpy of the reference samples.....	37
Table 9.	Vacancy Formation Energy as a Function of Cr Concentration.	38
Table 10.	Energetics of Self-Interstitial Samples.....	39
Table 11.	Mixed Interstitial Energetics in eV.	41

THIS PAGE INTENTIONALLY LEFT BLANK

ACKNOWLEDGMENTS

The author would like to thank Dr. Craig Smith and Dr. Xavier Maruyama on their mentorship and leadership, Dr. Alfredo Caro and Dr. Magdalena Serrano de Caro of Lawrence Livermore National Laboratory, who spent countless hours advising and guiding the research process.

THIS PAGE INTENTIONALLY LEFT BLANK

I. INTRODUCTION

The Fe-Cr alloys are considered for use as structural materials for Generation IV advanced nuclear designs. High doses of neutron irradiation cause vacancies and interstitials to form in the steel matrix. The most accurate approach for evaluating formation energies of point defects is numerical integration based on the first principles of quantum mechanics. However, due to the computational requirements posed by this method, it is prohibitive to use it for large scale simulations. It is therefore necessary to provide an approximation of *ab initio* results using Molecular Dynamics and Monte Carlo methodologies coupled with an adequately descriptive semi-empirical many body potential for alloys. The potential evaluated in this work is based on combining recent *ab initio* results with thermodynamic properties to describe formation energy as a function of local composition. This thesis seeks to answer the following questions:

- 1. Determine the extent to which this potential adequately approximates results obtained by *ab initio* calculations in pure elements.**
- 2. Determine how formation energies of point defects vary as a function of Cr concentration; determine their mutual relationships and stability in all possible configurations.**

In order to answer these questions, simulations were conducted using the Lawrence Livermore National Laboratory's massively parallel super-computing hardware and a suite of publicly available and custom designed materials science software solutions.

The calculations of this thesis show that reasonable predictions can be obtained using the potential described in this work. Formation energies of point defects in pure elements and as a function of Cr concentration and heretofore unexpected behavior of formation energies versus Cr concentration have been discovered.

THIS PAGE INTENTIONALLY LEFT BLANK

II. BACKGROUND

A. HISTORY OF NUCLEAR POWER

The use of nuclear power for energy generation traces its origins to the volatile times preceding World War II. The theoretical basis for fission was laid by Otto Hahn and Fritz Strassman in the German periodical *Naturwissenschaften* in January 1939, where they reported that an isotope of barium was produced by neutron bombardment of uranium. A knowledge network formed connecting Otto Robert Frisch and Lise Meitner, German scientists escaping Hitler's rule to Denmark, with Niels Bohr who was on his way to visit Albert Einstein at Princeton. Once the information got to Princeton which had become a Mecca for theoretical physics when Dr. Einstein joined its Institute for Advanced Studies, it set off a "chain reaction" in the scientific community. By the end of the year over a hundred papers on the subject of fission had been published in *Physical Review* and the concept of a sustainable chain reaction was grounded in theory [1].

The engineering required to sustain and control a chain reaction was, at the time, far from trivial. Nonetheless, the first artificial nuclear reactor, Chicago Pile 1 (CP-1), was built and reached criticality on December 2nd, 1942 at the underground racquetball courts at the University of Chicago [2].

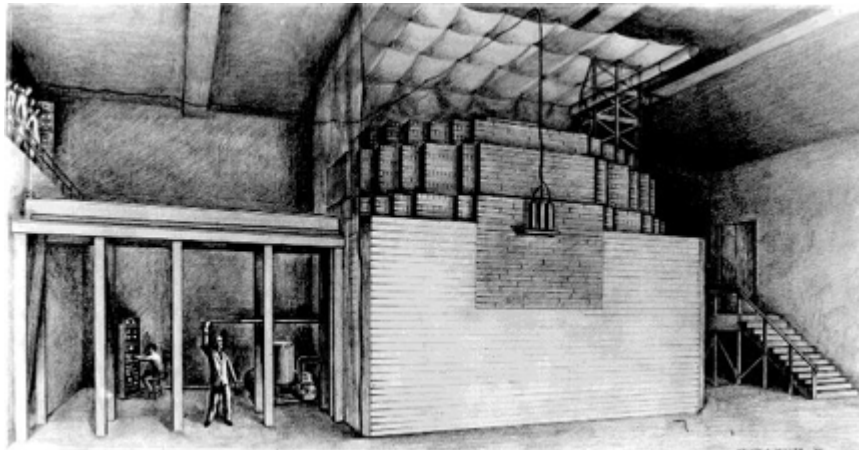


Figure 1. Drawing of Chicago Pile 1 [3]

At the time there was no possibility of enriching the nuclear fuel, so natural uranium had to be used, which contains only about 0.7 % of the highly fissionable

uranium-235 isotope, with the remainder consisting of the more stable uranium-238. It was therefore necessary to use large quantities of highly purified graphite as neutron moderation material. The moderator was necessary to slow down the high energy neutrons produced by fission to an energy range where they would be much more easily absorbed by U-235 around .025 eV, roughly the same temperature as that of the surrounding material; hence the name “thermal.” [4] The fission cross section of U-235 as a function of neutron energy is shown in Figure 2.

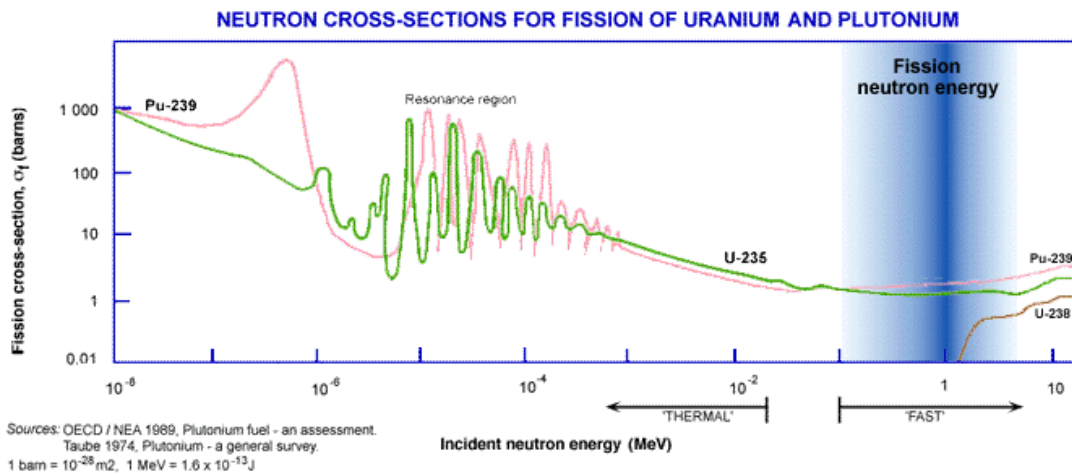


Figure 2. Neutron Cross-Sections for Fission of Uranium and Plutonium [5]

As we can see from Figure 2, neutrons produced by fission will fall within the energy range of .1 MeV to 5 MeV, but uranium-235 has the highest fission cross section at energies well below that value. The “moderator” is therefore used to slow down the fission-produced neutrons and increase their probability of causing fissions. The “moderator” is usually a highly purified substance, generally deuterium (in the form of heavy water), beryllium, or graphite for natural uranium reactors. These materials do not absorb neutrons easily (they have a low absorption cross section), but their nuclei are light enough that neutrons collide inelastically, transferring their kinetic energy to the moderator and therefore slowing down in the energy spectrum towards the energies which make them more likely to cause further fissions [4]. A diagram showing a typical moderated chain reaction is shown in Figure 3:

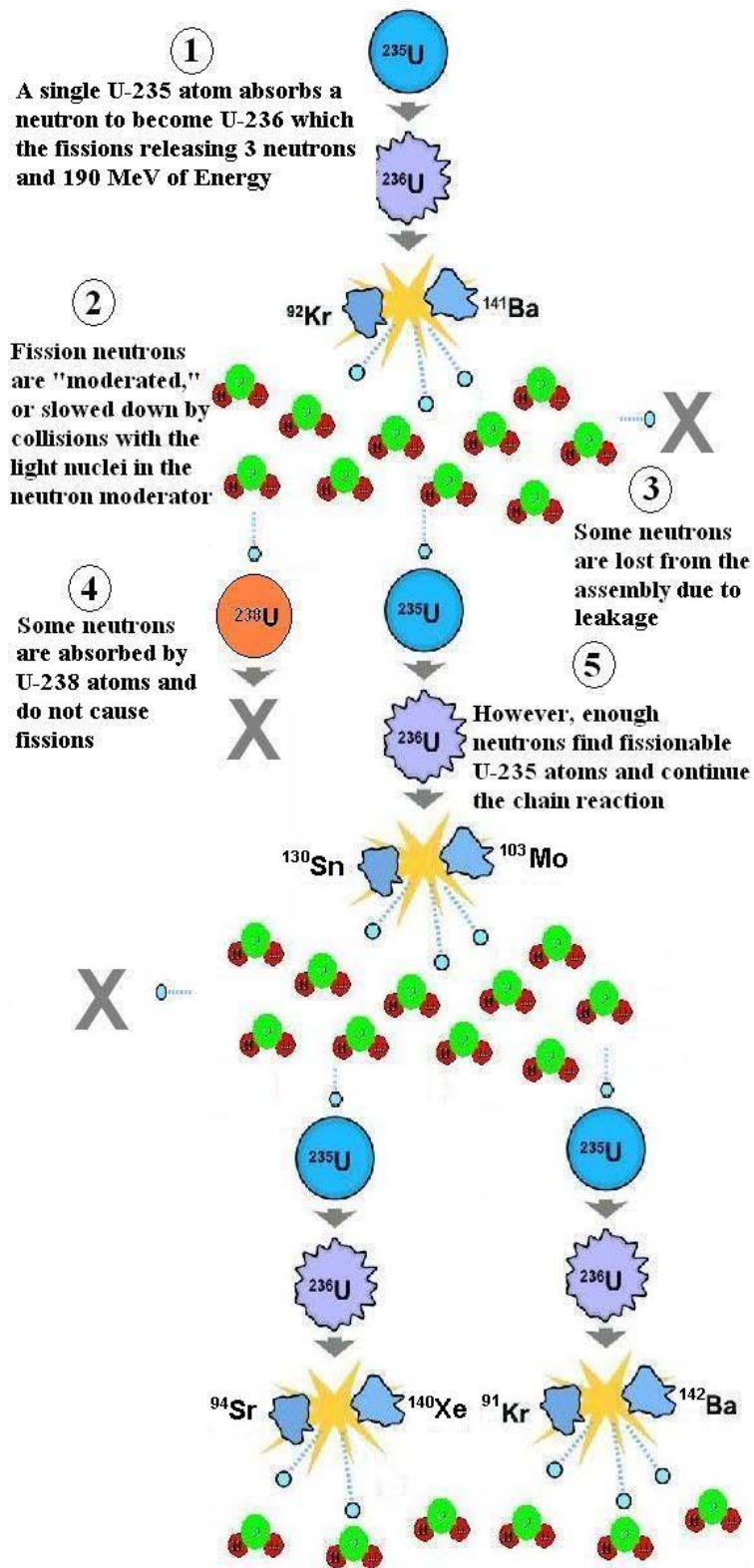


Figure 3. A Moderated Chain Reaction

Once it became possible to enrich uranium, therefore increasing the percentage of uranium 235 in the fuel, it became possible to utilize light water for both moderation and cooling of large scale engineering systems. This advance generally heralded the arrival of the next generation of nuclear reactors. This generation of reactors was, for the most part, typified by pressurized water reactors (PWR) and boiling water reactors (BWR) in the West and the VVER/RBMK reactors in the former Soviet Union and satellite states. Canada, due to the abundance of natural uranium ore, opted for a heavy water reactor design (CANDU) which used natural rather than enriched uranium. All of these systems are considered to be second generation nuclear reactors, two common threads of which are the unique design and features of each reactor unit and their thermal-neutron based operating cycle [6].

B. FUTURE DIRECTIONS IN NUCLEAR POWER

The newly emerging, third generation of reactor designs are equipped with advanced features such as safety systems incorporating passive energy dissipation or natural processes, simplifying their design and allowing them to cope with malfunctions without the need for operator action. Even though these designs are still confined to the thermal end of the fission cross section, third generation designs show some marked improvements when compared to their second generation cousins. Some of those are listed below:

- a standardized design for each type to expedite licensing, reduce capital cost and reduce construction time,
- a simpler and more rugged design, making them easier to operate and less vulnerable to operational upsets,
- higher availability and longer operating life - typically 60 years,
- reduced possibility of core melt accidents,
- minimal effect on the environment,
- higher burn-up to reduce fuel use and the amount of waste [7].

After the Three Mile Island accident, United States imposed a self-imposed moratorium on building new nuclear reactors. While third generation reactors have been built in Japan, Taiwan and Europe, this technology stagnated in the United States.

In 2000, however, eleven world nations formed The Generation IV International Forum (GIF), a research and development consortium tasked with leading the way toward innovative nuclear energy systems. Based on eight far-ranging technology goals, Generation IV nuclear energy systems are aimed at achieving nuclear energy's potential worldwide. The objective is a new generation of nuclear energy systems that:

- advance nuclear safety;
- address nuclear nonproliferation and physical protection issues;
- are competitively priced, and
- minimize waste and optimize natural resource utilization.

Among the six most promising designs for Generation IV, three are thermal neutron spectrum systems (the Very-High-Temperature Reactor (VHTR) and Supercritical-Water-Cooled Reactor (SCWR)) with coolants and temperatures that enable hydrogen or electricity production with high efficiency, and three are fast neutron spectrum systems (the Gas-Cooled (GFR), the Lead-Cooled (LFR), and the Sodium-Cooled (SFR) fast reactors) that will enable more effective management of actinides through recycling of most components in the discharged fuel. [8]

A significant change in Generation IV relative to previous reactor generations is the planned commercialization of fast spectrum systems. A fast spectrum neutron reactor is a reactor in which the chain reaction is sustained by fast neutrons without significant thermalization. Such a reactor needs no neutron moderator, but must generally use fuel that is relatively rich in fissile material when compared to that required for a thermal reactor. A diagram outlining the differences between fast and thermal spectrum processes is shown in Figure 4.

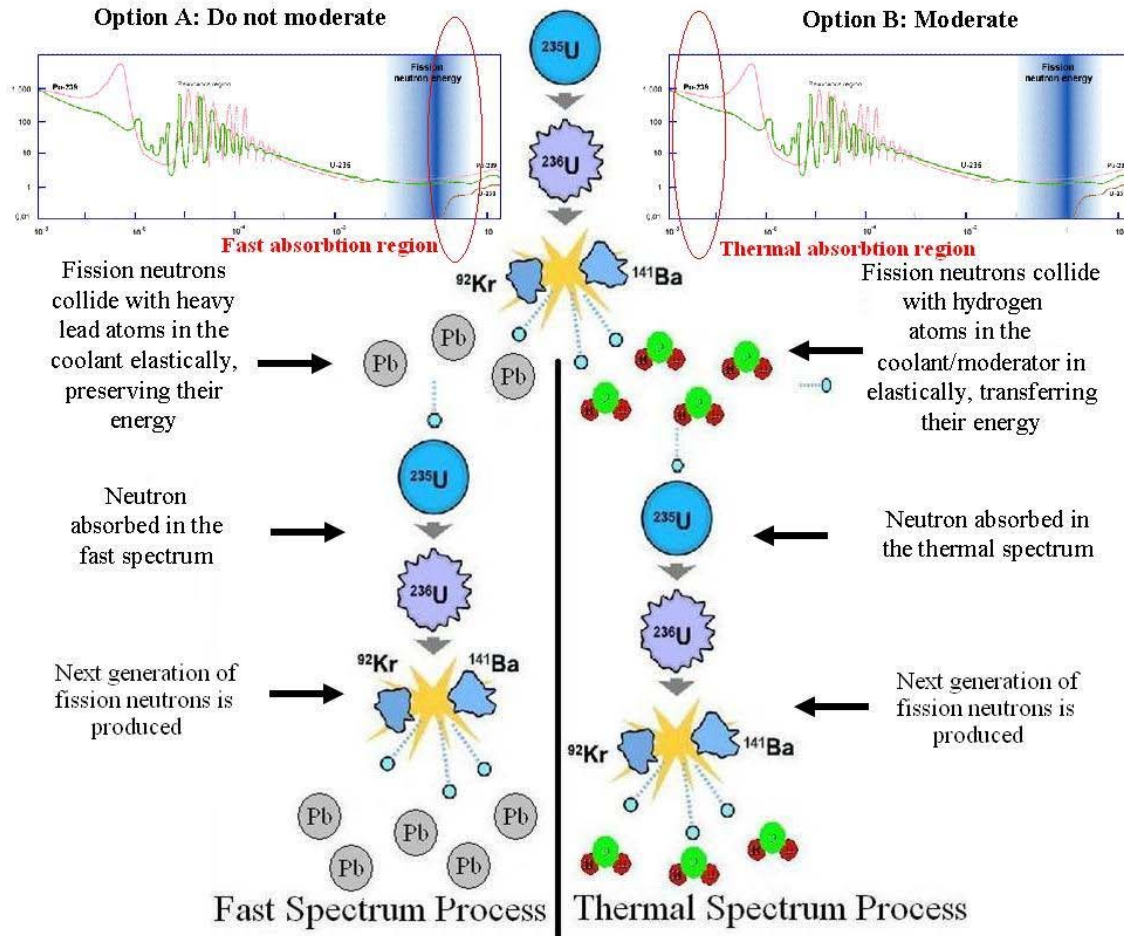


Figure 4. Overview of Differences Between Fast and Thermal Absorption Processes

Because parasitic absorption in the moderator can result in a major loss of neutrons in a thermal reactor, a fast reactor has an inherently superior neutron economy; that is, there are excess neutrons not required to sustain the chain reaction. These neutrons can be used to produce extra fuel, as in the fast breeder reactor, or to transmute long half-life waste to less troublesome isotopes, such as in the Super Phénix reactor near Cadarache in France, or in some combination of these two purposes [9]. An overview of nuclear energy development is shown in Figure 5:

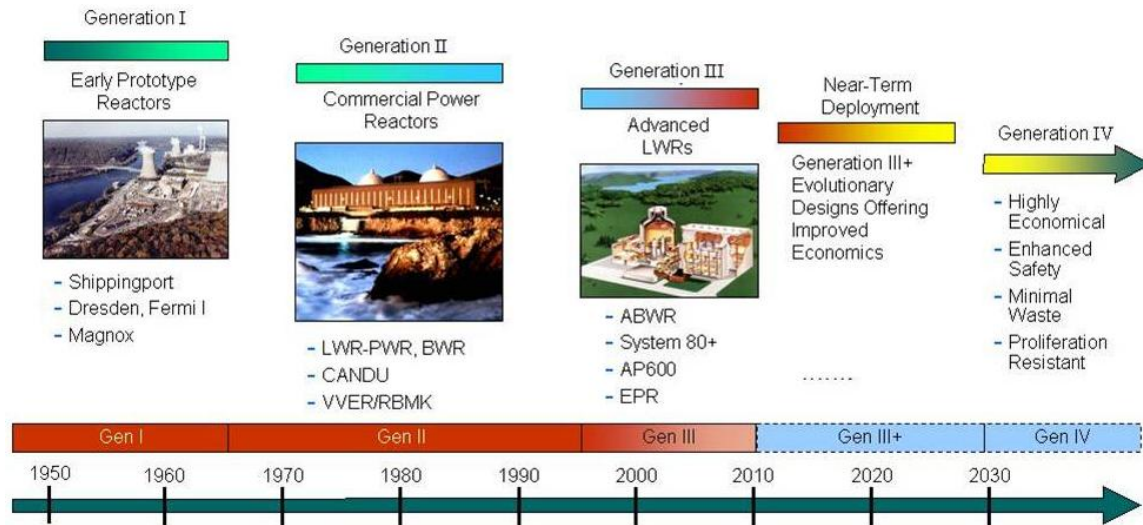


Figure 5. Overview of Reactor Technology Development [10]

C. FAST SPECTRUM NUCLEAR REACTOR DESIGN FEATURES

An example of a fourth generation system currently under development is a Lead-Cooled Fast Reactor (LFR), which features a fast-spectrum lead or lead/bismuth eutectic liquid metal-cooled reactor with a closed fuel cycle. The Pb coolant is a poor absorber of fast neutrons and this enables the realization of improved sustainability and fuel cycle benefits. Pb does not interact vigorously with air, water/steam, or carbon dioxide, eliminating concerns about exothermic reactions. It has a high boiling temperature, so the prospect of boiling or flashing of the ambient pressure coolant is realistically eliminated. The LFR is cooled by natural convection with a reactor outlet coolant temperature of 550 °C, possibly ranging up to 800 °C with advanced materials. The higher temperature enables the production of hydrogen by thermochemical processes [11]

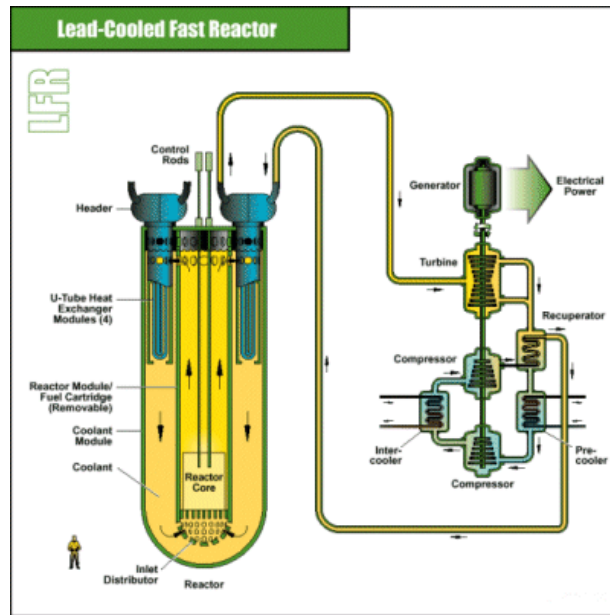


Figure 6. Lead-Cooled Fast Reactor Diagram [10]

Additionally, due to its neutron economy, an LFR can be designed in such a manner as to behave like a converter or even a breeder reactor, therefore enabling the conversion of the uranium 238 isotope into fissionable plutonium 239. A neutron captured by uranium 238 results in the formation of uranium 239, which has a half life of about 23 minutes and decays into neptunium 239 through beta decay. Neptunium 239 has a half life of 2.4 days and then decays into plutonium 239, also through beta decay [12]. The added benefit of the high neutron flux and fast spectrum core design is the ability of the LFR to serve in the actinide management role. [13]

Since the fission of fuel materials initially present in the core creates more new fuel (plutonium 239) from uranium 238, as a side product of fission, a properly designed reactor core can significantly extend the time between refueling, or indeed eliminate it altogether. An advanced reactor design that maximizes this property is the Small, Sealed, Transportable, Autonomous Reactor (SSTAR), currently under development by Lawrence Livermore and Argonne National Laboratories [11].

D. SSTAR PROGRAM OVERVIEW

The objective of the SSTAR program is to create a sealed reactor that can be delivered to a site, left to generate power for up to 30 years, and retrieved when its fuel is spent. The potential for nuclear proliferation would be minimized by sealing the cartridge core inside a tamper proof cask. The reactor would be monitored and operated autonomously with a satellite link to a national authority or international authorities overseeing the reactors. The system would include passive safety features such as a fast spectrum core with a strong reactivity feedback that enables autonomous load-following and provide passive power shutdown in case of a loss-of-coolant accident, as well as natural circulation flow of the Pb coolant. This is a critical issue, as the reactor's primary market is thought to be in undeveloped or underdeveloped regions of the world, where it would operate with almost full autonomy. This marketing strategy also provides the reasoning for the small size of the reactor, since conventional nuclear stations typically produce about a gigawatt of electricity, which would overwhelm the distribution grid in a developing country, therefore wasting much of the installed power [14].

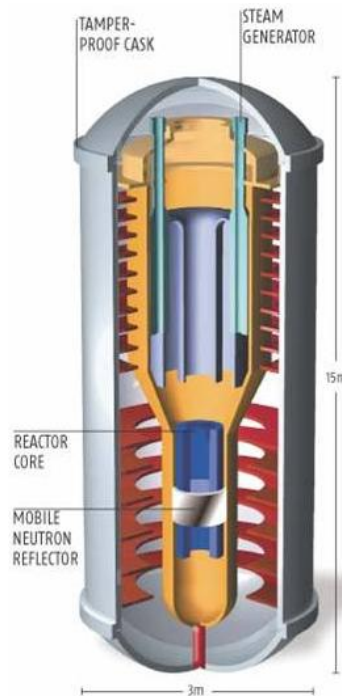


Figure 7. Diagram of a Potential SSTAR Design [14]

The nominal SSTAR design (20 MWe/ 45 MWt) is 18 meters tall and 3.2 m in diameter, which enables it to be easily moved by barge or rail. The producer would be responsible for delivering the sealed unit by ship and truck and installing it at the operating location. At the end of its regular operating life, the old reactor would be removed for recycling or disposal, and a replacement system would be deployed. [14]



Figure 8. SSTAR Deployment [14]

SSTAR would be coupled with an S-CO₂ gas turbine Brayton cycle power converter, which enables the reactor to operate with a higher efficiency when compared to the traditional Rankine saturated steam cycle. This modification is enabled by the higher core temperatures in the LFR design, attainable with the primary Pb coolant and highly enriched transuranic (TRU) nitride fuel in ¹⁵N in a compact core. The temperatures in consideration are 650°C peak cladding temperature and 561°C core outlet temperature for a 405°C core inlet temperature [13]. However, the advantages of this design face a critical limitation on the lifetime of this and other Generation IV reactor designs from the material corrosion which results from radiation damage to structural materials

III. MOTIVATION

A. RADIATION DAMAGE

Fission-emitted neutrons carry with them up to 5 MeV of energy. Continuous neutron bombardment of structural materials exposed to such high energy neutron radiation results in introduction of defects within the material's crystalline lattice. The inelastic collisions between the impacting neutrons and the structural atoms cause energy to be transferred to the atoms. Since the structural materials are, for the most part, comprised of stable elements, the system response to the higher energy state of the atom is its displacement from its original site within the lattice. This disorder within the perfect crystal lattice is referred to as a Frenkel disorder [15]. It results in the formation of a Frenkel pair of defects, where there is a single vacancy and a single interstitial within the structure [15].

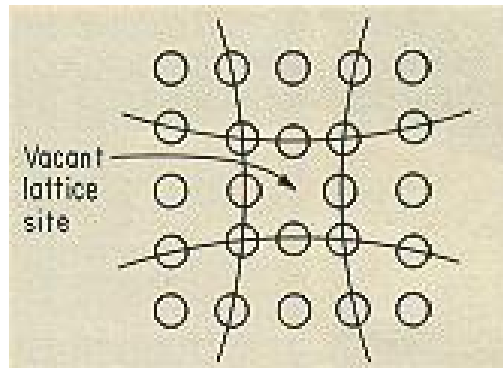


Figure 9. Vacancy Site in a Crystalline Structure [16]

Vacancies are sites which would normally be occupied by an atom but which as a result of the displacement are unoccupied. If a neighboring atom moves to occupy the vacant site, the vacancy moves in the opposite direction to the site which used to be occupied by the moving atom. The stability of the surrounding crystal structure guarantees that the neighboring atoms will not simply collapse around the vacancy. In some materials, neighboring atoms actually move away from a vacancy, because they can better form bonds with atoms in the other directions [15].

Interstitials are atoms which occupy a site in the crystal structure at which there is usually not an atom. They are generally high energy configurations. There are two basic kinds of interstitials: Intrinsic and extrinsic interstitials. **Intrinsic interstitials** are interstitial atoms of the same kind as the atoms of the crystal ("**self-interstitials**"). They are practically nonexistent in elemental crystals (that are found in all metals) with the significant exception of **Si**, where intrinsic interstitials play an important role in diffusion and microdefect formation. **Extrinsic interstitials** are interstitial atoms of a foreign (extrinsic) type, e.g. **C** in **Fe** or **O** in **Si** ("**mixed interstitials**"). They may diffuse directly through the lattice (i.e., without the help of vacancies) and play an important role in many technically relevant materials [15]

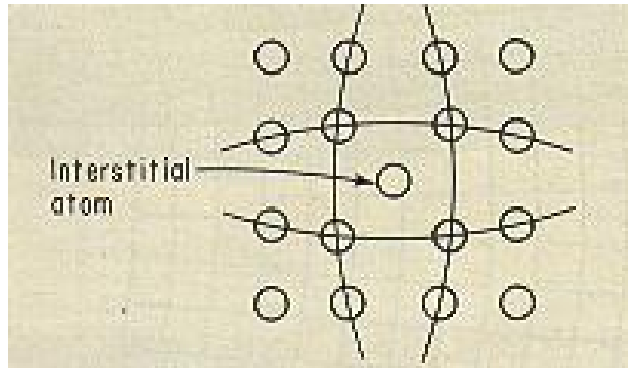


Figure 10. Interstitial Atom in a Crystal Lattice [16]

Complexes can form between different kinds of point defects. For example, if a vacancy encounters an impurity, the two may bind together if the impurity is too large for the lattice. Interstitials can form 'split interstitial' or 'dumbbell' structures where two atoms effectively share an atomic site, resulting in neither atom actually occupying the site [15]. These interstitial pairs can be oriented in three possible directions:

- $\langle 100 \rangle$: Atoms displaced in only in one axis as shown in Figure 11;

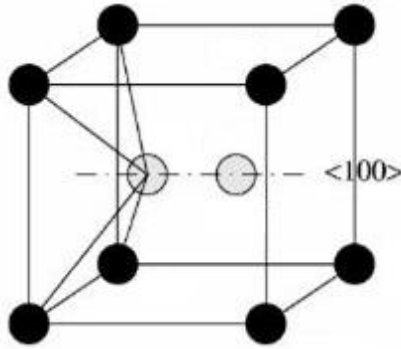


Figure 11. $\langle 100 \rangle$ Interstitial [17]

- $\langle 110 \rangle$: Atoms displaced in two axes as shown in Figure 12; and

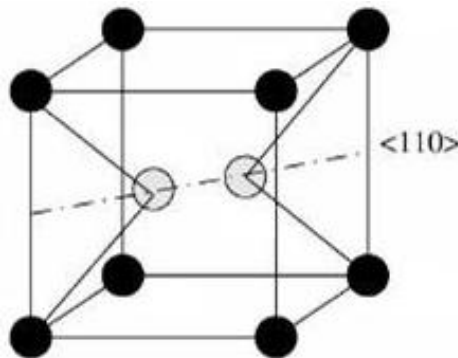


Figure 12. $\langle 110 \rangle$ Interstitial [17]

- $\langle 111 \rangle$: Atoms displaced in all three axes as shown in Figure 3-8.

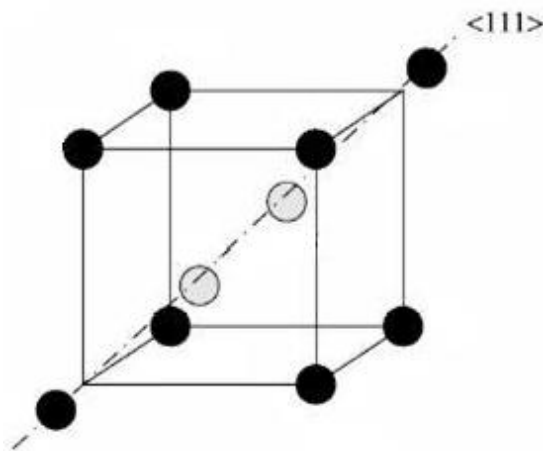


Figure 13. $\langle 111 \rangle$ Interstitial [17]

The result of a single neutron collision is not a single defect; on the contrary the interaction of a single 1 MeV neutron with an atomic nucleus transfers up to about 100

keV to the primary knock-on atom (PKA) of iron. Some of this recoil energy is lost to interactions with the electron cloud, resulting in a somewhat lower kinetic energy that is dissipated in atomic collisions. The PKA kinetic energy is then transferred by numerous subsequent collisions and resultant displacements, producing further generations of recoiling atoms at lower energies. The process terminates when the kinetic energy of the n th-generation of recoils falls below that needed to cause additional displacements [18]. Closely spaced interstitials and vacancies quickly recombine and only about one-third of the initial displacements survive. Typically, this leaves a vacancy-rich cascade core, surrounded by a shell of interstitials. The majority of interstitials quickly cluster to form small, disc-shaped features that are identical to small dislocation loops [19]. Along with interstitials, these loops are very mobile. Diffusion of individual interstitials and loops within the cascade region causes additional recombination prior to their rapid long-range migration (unless they are strongly trapped by other defects or solutes). Although they are less mobile than interstitials, vacancies also eventually diffuse. Through a series of local jumps, the vacancies and solutes in the cascade quickly begin to evolve to lower energy configurations, forming small, three-dimensional clusters, while others leave the cascade region [19]. The small clusters are unstable and can dissolve by vacancy emission. However, the small clusters also rapidly diffuse and coalesce with each other, forming larger nanovoids, which persist for much longer times. Solute atoms bind to the vacancies and segregate to clusters. The vacancy emission rate is lower from vacancy-solute cluster complexes. Small solute clusters remain after all the vacancy clusters have finally dissolved. Expressing damage exposure, or neutron dose, in terms of displacements-per-atom (dpa) partially accounts for the effect of the neutron energy spectrum on the generation of cascade defects and the net residual defect production scales with dpa [20].

B. MACRO-LEVEL EFFECTS OF RADIATION DAMAGE

This time evolution of microscopic defects results in the following emergent macroscopic material behaviors:

- **Volumetric Swelling:** irradiated material will display volumetric expansion in all axes. This results from lattice parameter elongation and

void formation [21]. An example of radiation induced swelling of austenitic steel is shown in Figure 14



Figure 14. Radiation Induced Swelling [21]

- **Irradiation Creep:** a time-dependent, constant rate mechanical deformation of material occurring slowly at stresses below the ultimate tensile stress. Vacancies cause biased absorption of interstitials at dislocations leading to net dislocation climb [22]. An example of irradiation creep is shown in Figure 15.



Figure 15: Irradiation Creep of Nuclear Fuel Pin Cladding [23]

- **Radiation hardening and embrittlement.** This is a second order phenomenon which is caused by the slipping over the dislocation-linked clusters of point defects. This leads to decreased plasticity of the irradiated material and ultimately greater proclivity towards rapid catastrophic fracture generation. These effects become even more pronounced as the ambient temperature increases [18].

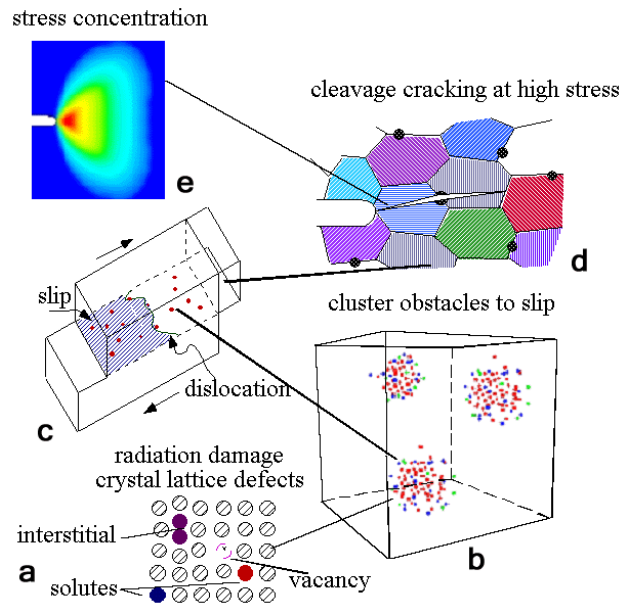


Figure 16: Diagram of Material Hardening and Embrittlement Evolution [18]

C. MATERIAL ISSUES FOR GENERATION IV NUCLEAR ENERGY SYSTEMS

The fact that nuclear materials are subject to radiation damage is well known from the many reactor years of operation accumulated in operation of Generations I and II systems. However, when we compare the operating conditions present in early generations of nuclear reactors to those projected for Generation IV and other advanced nuclear applications, we see that the operating environment adversity significantly increases.

	Fission (Gen. I)	Fission (Gen. IV)	Fusion (Demo)	NASA space react.
Structural alloy maximum temperature	<300°C	500-1000°C	550-1000°C	~1000°C
Max dose for core internal structures	~1 dpa	~30-100 dpa	~150 dpa	~10 dpa
Max transmutation helium concentration	~0.1 appm	~3-10 appm	~1500 appm (~10000 appm for SiC)	~1 appm
Coolants	H ₂ O	He, H ₂ O, Pb- Bi, Na	He, Pb-Li, Li	Li, Na, or He-Xe
Structural Materials	Zircaloy, stainless steel	Ferritic steel, SS, superalloys, C- composite	Ferritic/ martensitic steel, V alloy, SiC composite	Nb-1Zr, Ta alloys, Mo alloys, superalloys

Table 1. Operating Conditions for Advanced Nuclear Applications [24]

This increase in adversity, as seen from Table 1, make the materials previously used for nuclear applications, namely austenitic steels (such as 316-L), no longer suitable for advanced applications. Therefore, ferritic-martensitic steels, such as HT-9, T-91 and EP823 have to be considered. The chemical composition of the ferritic-martensitic steels is compared to an example of austenitic steel in Table 2.

Material	C	Si	Mn	S	P	W	Cr	Ni	Mo	V	Nb	N	Ti	Fe
HT-9	0.2	0.25	0.5	---	---	0.5	12	0.56	1	0.3	---	---	---	84.7
T-91	0.1	0.4	0.45	---	---	---	9	---	1	0.2	0.08	0.05	---	88.7
EP823	0.18	1.05	0.6	---	0.012	0.65	11.4	0.7	0.67	0.4	0.2	---	0.03	84.1
316-L	0.035	0.08	2.0	0.03	0.040	---	16	10	2	---	---	---	---	69.6

Table 2. Chemical Composition of Potential Generation IV Structural Materials [25]

We can see that a common thread among the materials considered is that they are all variants of iron-chromium (Fe-Cr) alloy, but the following are the practical reasons why these materials were selected:

1. Unlike stainless steel which starts to swell almost immediately after being irradiated, Fe-Cr alloys exhibit a delay in swelling, wherein they do not exhibit that property until receiving 100 dpa of radiation damage.
2. Fe-Cr alloys perform well at high temperatures and pressures required for operation of advanced nuclear reactors, and they have favorable rates of corrosion when exposed to the elements intended for use as coolants (Pb, Bi, Na).
3. Their welding properties are well known and there is experience with high temperature helium embrittlement [26].

However, despite all these favorable properties, the behavior of defect clustering resulting in irradiation creep, hardening and embrittlement is poorly understood in Fe-Cr alloys. Considering that these behaviors are known to occur in materials used in earlier reactor designs, which operate in much more benign conditions, it becomes imperative to thoroughly understand them. Additionally, when we take into account the intended life-time of a Generation IV system (around 60 reactor years) and that some designs (such as SSTAR) are intended to operate autonomously for extended periods of time, it is clear that our ability to model the time evolution of Fe-Cr alloys is critical for safe operation of these systems.

D. MULTI-SCALE APPROACH TO MATERIAL SCIENCE MODELING

Since radiation induced defects occur at the atomistic level, the most accurate method of calculating their energetic properties is to solve the Schrödinger equation (or Dirac equation, if relativistic effects are important) in its many-body electron form. However, this is an exceptionally difficult and computationally intensive process, as the currently “standard” model for condensed matter physics, the Density Functional Theory (DFT) using Local Density Approximation (LDA), is currently limited to 100-1000 atoms. The largest DFT simulation to date is 1080 B atoms (with 3840 electrons simulated) on Lawrence Livermore National Laboratory’s 2000 CPU Linux cluster [23]. While the DFT approach is generally successful in predicting structures and macroscopic properties, it under-predicts band gap energies, over-predicts lattice parameters, and predicts wrong ground states for some magnetic systems (e.g., Fe). Nonetheless, for the

purposes of material and reactor engineering, requiring time evolution of macro scale behaviors such as void swelling, hardening, embrittlement, creep, stress corrosion cracking, the first-principles calculation is not suitable [27]. Therefore, in order to arrive at a successful time-evolved simulation of a finite structural element, several layers of approximation are necessary.

The multi-scale modeling approach to material science is only natural, because the introduction of defects, their evolution and mutual interaction and ultimately their effect on the mechanical properties of the material all occur on very broad timescales, as can be seen in Figure 17.

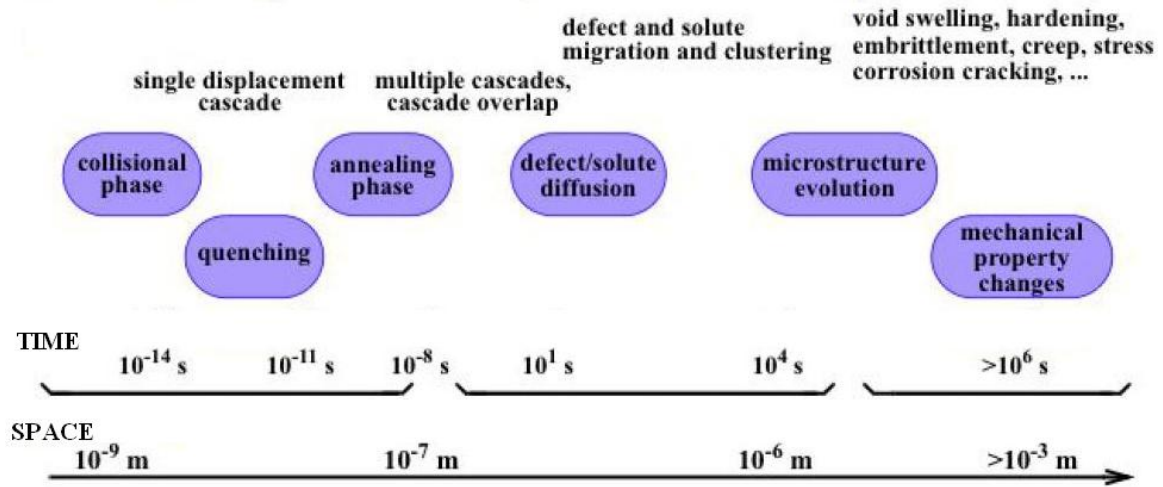


Figure 17. Temporal and Spatial Placement of Phenomena [23]

The modeling of these phenomena in a global sense is a chain of events in which the results of each previous step serve as the source of inputs and basis of comparison for the subsequent steps. Fitting the model at the next higher level of approximation is done by comparing its results for properties best modeled by the method on a finer scale. By using a bottom-up approach, based on first principles and built upon scale reversible models (when possible) starting from the sub-nanometer scale (where the building blocks of matter are established, hence providing material unity and technology integration), complete characterization of properties in materials and processes at different dimensional and time scales can be achieved. In addition, a sequence of experiments is designed to follow the modeling effort and validates the simulation result. A visual

description of the overall multi-scale modeling effort, complete with supporting experiments is shown in Figure 18.

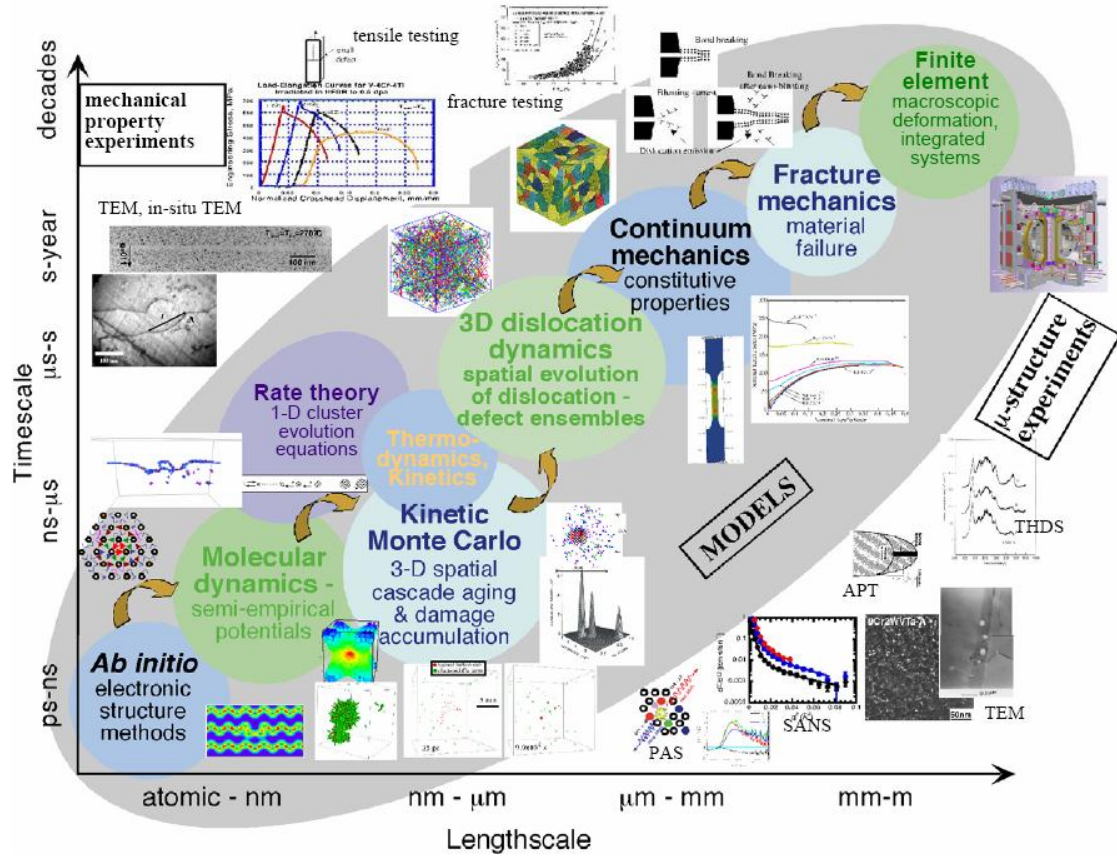


Figure 18. Global View of Multi-scale Material Modeling Effort [28]

IV. THEORY AND METHODOLOGY FOR COMPUTATION

A. INTRODUCTION

Modern materials science evolved from two basic elements--metallurgy and alchemy--and has over the period of the last couple of decades greatly expanded its field of study. Its natural complexity had, for a very long time, kept its progress in check as the difficult physical concepts could only be applied to idealized, pure forms. Nonetheless, Moore's Law compounding of computer power has recently enabled numerical simulation of increasingly complex systems. While the most exact calculations are based on first principles of quantum mechanics, alternatively referred to as *ab initio* calculations, their sheer complexity has yet to be conquered by Moore's Law. The complexity of these calculations is clear to anyone who has ever taken an introductory course in quantum mechanics, which culminates in solving the Schrödinger Equation for a hydrogen atom. However, since most useful materials contains significantly more complex elements, the difficulty is compounded as it becomes necessary to solve Schrödinger's many-electron equation in the following form:

$$H\Psi = [T + V + U] \Psi = \left[\sum_i^N -\frac{\hbar^2}{2m} \nabla_i^2 + \sum_i^N V(\vec{r}_i) + \sum_{i<j} U(\vec{r}_i, \vec{r}_j) \right] \Psi = E\Psi \quad (1)$$

Where H is the electronic molecular Hamiltonian, N is the number of electrons and U is the electron-electron interaction. The operators T and U are so-called universal operators as they are the same for any system, while V is system dependent or non-universal. In essence, the greatest complexity in *ab initio* methods arises from the many-body interaction term U . While there are many clever methods for reducing the computational power required to solve this equation for a complex system, those remain a discussion for another day. A powerful approach has been developed in Ref. [29], that uses classic interatomic potentials and incorporates *ab initio* and experimental results, in order to enable the study of crystalline defects and their long range interactions on a much larger scale.

B. THE MANY-BODY POTENTIAL

The models generally used for this work are colloquially known as “many-body” potentials, and can be globally grouped in two categories: the embedded-atom models and the second moment approximation [30]. However, the issue facing material modelers for advanced nuclear applications is that the overwhelming body of work in this field is focused on either pure elements or intermetallic compounds; only a few authors address concentrated alloys.

The methodology used for this work was developed by Dr. Alfredo Caro, et al. of the Lawrence Livermore National Laboratory, first published in the Physical Review Letters article of August 2005 [29]. The objective of this methodology is to address arbitrarily complex systems of concentrated alloys with complex heat of formation. What makes this work especially appropriate is that this methodology is applied to Fe-Cr alloys which are of interest for advanced nuclear applications.

The “many-body” potentials are based on the summation of atom energies which provides the total energy of the system. The atom energies are themselves composed of two contributions; namely, embedding and pair potential terms. For heteroatomic systems, such as binary alloys composed of elements A and B, this reads:

$$E = \sum_i^N \left[F_{\alpha_i} \left(\sum_{j \neq i} \rho_{\alpha_i \beta_j}(r_{ij}) \right) + \frac{1}{2} \sum_{j \neq i} V_{\alpha_i \beta_j}(r_{ij}) \right], \quad (2)$$

where α and β stand for elements A and B sitting at sites i and j within the crystalline lattice, F ’s are the embedding functions for either type of element, and V ’s and ρ ’s are the pair potentials and densities between α - β pairs. The functions $\rho_{\alpha\beta}$ and $V_{\alpha\beta}$ therefore describe the properties of the alloy. The variety in expressions of embedding energies, densities, and pair potentials encompasses a great similitude of models.

The greatest issue in application of this model to the case of Fe-Cr is that unlike other binary alloys, its formation energy is not a symmetric function. Instead, in the case of Fe-Cr this function is highly nonsymmetrical and it even changes sign at low Cr composition [35], as seen in figure 19.

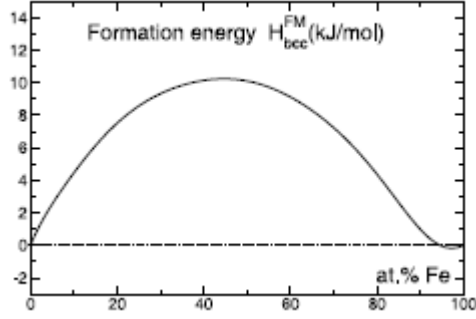


Figure 19. Ab Initio Calculations of Fe-Cr Mixing Enthalpy [35]

Therefore, in contrast to the binary alloys with symmetric formation energy such as Au-Ni and Fe-Cu, the standard approach using a cross pair potential term is not good enough to reproduce the properties of the systems. By using the potentials already described in the literature, adjusting the alloy term in equation (2) and focusing on nonlinearities built upon the pair potential cross term alone, this methodology manages to create a model which successfully departs from ideality and matches the heat of formation behavior as described by Par Olsson et al. in [35] and as shown in Figure 20.

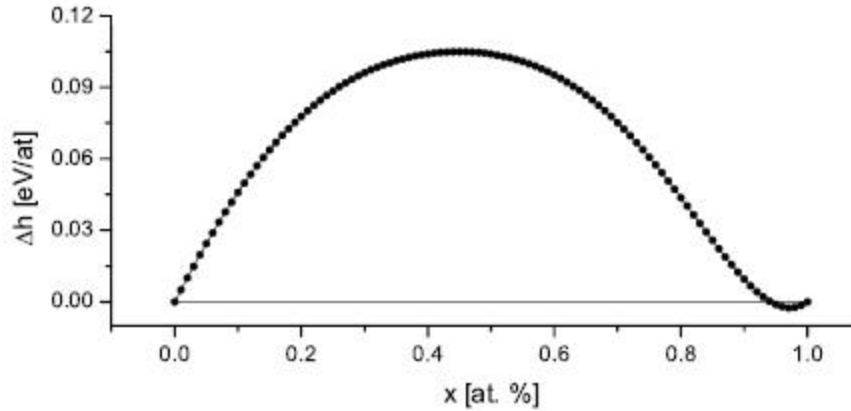


Figure 20. Formation Energy of the Alloy as Predicted by the Potential Used in This Work [29]

C. THE FREE ENERGY EXPRESSION

The free energy model uses an effective representation of two pure element potentials as reported by Mendelev for Fe [36] and Wallenius for Cr [37], with normalized densities, which for $\alpha = A, B$ reads

$$\begin{aligned}
\rho_\alpha &= \rho_\alpha^o / \varrho_{\alpha,eq}^o, \\
F_\alpha(\varrho_\alpha) &= F_\alpha^o(\varrho_\alpha^o) - F_\alpha^{o'}(\varrho_{\alpha,eq}^o) \varrho_\alpha^o, \\
V_{\alpha,\alpha}(r) &= V_{\alpha,\alpha}^o(r) + 2F_\alpha^{o'}(\varrho_{eq}^o) \rho_\alpha^o(r),
\end{aligned} \tag{3}$$

where the superscript o stands for original, $\hat{\rho}_{\alpha,eq}^o$ for the density on a lattice site at equilibrium $[\sum_{j \neq i} \rho_{\alpha_i}(r_{ij}^{eq})]$, and the prime $'$ for derivative. These transformations do not alter the properties of the pure elements but have the advantage of minimizing the contribution of the embedding term to the formation energy of the alloy, thus enabling unrelated pure element potentials to be combined in this alloy description, as shown by the free energy of a random solution alloy with composition x at temperature T in equation 4:

$$g(x, T) = g_{\text{ref}}(x, T) + g_{\text{mix}}(x, T) + \Delta g(x, T), \tag{4}$$

where g_{ref} is the compositional weighted free energy of the pure components, g_{mix} is the free energy contribution from the entropy of mixing for a random alloy, and Δg is the excess Gibbs energy of mixing, which, when expressed by a Redlich-Kister expansion [38] reads

$$\Delta g(x, T) = x(1 - x) \sum_{p=0}^n L_p(T)(1 - 2x)^p, \tag{5}$$

where L_p is the p -th order binary interaction parameter. This parameter is also the object of two major simplifications in this methodology, as it is generally a function of temperature. Therefore, in order to reduce the complexity of the description we neglect the excess vibrational entropy and assume that the formation energy does not depend on T . This leads to a simplified version of equation (5).

$$\Delta g(x, T) \cong \Delta H(x) = x(1 - x) \sum_{p=0}^n L_p(1 - 2x)^p. \tag{6}$$

The factors for the Redlich-Kister expansion come from the Par Olsson *ab initio* calculations [35] and are given in the table below.

L_0	L_1	L_2	L_3	L_4
0.41566	0.0814134	-0.0101899	0.267659	-0.248269

Table 3. Values of the Redlich-Kister expansion coefficients for Eq. (6)

D. THE CROSS PAIR POTENTIAL

The functional form of the cross potential is based on the analytic mode of the alloy in which the species that sits on site i can be either A or B, but both are embedded in the same average environment, as discussed by Ackland and Vitek [31]:

$$\begin{aligned}
E^{\text{rand}} = & x_A^2 \sum V_{AA}(r_{ij}) + x_B^2 \sum V_{BB}(r_{ij}) \\
& + 2x_A x_B \sum V_{AB}(r_{ij}) + x_A F_A(\tilde{\rho}) + x_B F_B(\tilde{\rho})
\end{aligned} \tag{7}$$

where the $\tilde{\rho}$ is defined as

$$\tilde{\rho} = x_A \sum \rho_A(r_{ij}) + x_B \sum \rho_B(r_{ij}) \tag{8}$$

Therefore, the contribution of the embedding terms to the mixing energy, ΔE^{emb} , is

$$\begin{aligned}
\Delta E^{\text{emb}} = & x_A [F_A(\tilde{\rho}) - F_A(\tilde{\rho} = 1)] \\
& + x_B [F_B(\tilde{\rho}) - F_B(\tilde{\rho} = 1)].
\end{aligned} \tag{9}$$

Using a Taylor expansion of F around $\tilde{\rho}=1$ and using equation (3), it becomes clear that this contribution is quadratic in $(\tilde{\rho} - 1)$, and therefore small for small variations in $\tilde{\rho} - 1$ as seen in

$$\Delta E^{\text{emb}} = x_A F_A''(\tilde{\rho} = 1)(\tilde{\rho} - 1)^2 + x_B F_B''(\tilde{\rho} = 1)(\tilde{\rho} - 1)^2. \tag{10}$$

The specific potentials used for this study reduce the embedding term contribution to the formation energy down to ~ 1 meV/atom at $x = 0.5$, making it negligible in comparison to the target value of ~ 100 meV for Fe-Cr alloys [35]. This enables us to write down the energy contribution from the pair potential terms as follows,

$$\Delta E^{\text{pair}} = x(1 - x)\{2v_{AB} - (v_A + v_B)\}. \tag{11}$$

It is therefore assumed that: a) the nonlinearity is dependent only on the pair potential and b) V_{AB} is a function of both x and r , separable as a product of $h(x)u_{AB}(r)$, with the form,

$$V_{AB}(x, r) = h(x) \frac{1}{2} [V_{AA}(r) + V_{BB}(r)]. \quad (12)$$

The $h(x)$ is also a 4th order Reidlich-Kister polynomial, whose factors are obtained through global minimization of equation (7) using MathematicaTM, and listed in Table 4.

H_0	h_1	H_2	H_3	h_4
0.883644	-0.059302	0.644634	-1.342524	0.918932

Table 4. 4th Order Polynomial Coefficient for $h(x)$, as Obtained by Minimization

This methodological approach yields a formation energy curve indistinguishable from the target function obtained by the *ab initio* calculations of Par Olsson [35], as seen in Figure 19. Therefore, it can be concluded that it is reasonable to utilize this potential for modeling the formation energies of point defects in Fe-Cr alloys.

E. THE MOLECULAR DYNAMICS CODE

According to Ohno et al. [42], the method of classical molecular dynamics (MD) was first proposed by Alder and Wainwright in 1957. The essence of the approach comes from two assumptions: a) that there is a set of defined interatomic force functions or a potential, as we have shown in the beginning part of this chapter; and b) the numerical ensemble in which the number of particles N , the temperature T and the chemical potential μ are constant. If the above two statements are correct, the equation of motion for the atoms is the usual Newtonian equation

$$m_i \frac{d^2 r_i}{dt^2} = F_i, \quad F_i = -\nabla_i \sum_{j=1}^N V_{ij} \quad (13)$$

where m_i is the mass of the i -th particle, r_i its coordinate and F_i the force acting on it. The code solves this equation numerically and performs energy minimization of the ensemble, therefore achieving thermal equilibrium after a sufficient number of iterations. This in

turn provides us with the energetics of a sample in which all the atoms have achieved their least energetic state and are in a “relaxed” state.

One of the greatest limitations of the MD approach has been in coping with the effects of finite system size and presence of surfaces. In order to reduce these effects, the code uses periodic boundary conditions. With this approach, all the particles are placed inside a box, or a unit cell. If the particle goes outside the cell, it is brought back in from the opposite side of the cell. While this approach works marvelously with perfect crystal systems, introducing a disturbance such as a point defect creates problems because the code is inclined to see a “mirror image” of the defect across the periodic boundary conditions, therefore unintentionally creating a cascading effect of mutual influence.

One technique for minimizing the effects of finiteness of the simulated system is to sum the forces exerted on the i -th particle from all other particles inside a certain “sphere of influence” defined by the cut-off radius R_c centered on the particle. Of course this summation must be performed even if the particles are not in the same unit cell, but in the image cells [43]. Ideally, having an adequately large sample size in which the sphere of influence radius around the i -th atom does not encompass any atoms affected by the presence of its mirror image solves this problem.

THIS PAGE INTENTIONALLY LEFT BLANK

V. PROCEDURE AND RESULTS

A. RESEARCH PLAN

The thesis research was conducted according to the following schedule:

- Task 1: The Study of Defects in Pure Elements. The objective of this section of the thesis is to prove that the Caro potential [29] adequately approximates results obtained by *ab initio* calculations. This will be done by calculating formation energies of point defects in pure element samples and comparing those results against values available in literature, obtained through *ab initio* calculations.
- Task 2: Evaluating the Vacancy Energy of Formation. This section is aimed at evaluating the behavior of vacancy formation energy in samples with increasing chromium concentration. This will serve to define the specific energetics of this point defect for a range of Cr concentration in relation to a linear interpolation between vacancy formation energies in pure elements.
- Task 3: Obtaining the Formation Energies of Interstitials. In this section the research will focus on defining the behavior of formation energies as a function of Cr concentration for a variety of interstitial configurations, as well as exploring their relative relationships.

Put together, the scope of these results will serve to prove the applicability of this type of a semi-empirical potential for approximating the results of *ab initio* calculations and provide static and dynamic calculations on a scale currently unobtainable by *ab initio* simulation.

B. CHARACTERIZING THE PERFORMANCE OF THE CODE: THE STUDY OF DEFECTS IN PURE ELEMENTS

In order to benchmark the performance of the newly developed potential [29] against other available Fe and Cr potentials and methodologies, it was necessary to compare its prediction of formation energies for the 12 point defects types of interest:

- Single Vacancy in a pure Fe sample
- Single Vacancy in a pure Cr sample
- Self-interstitial (Fe-Fe) $\langle 110 \rangle$ in a pure Cr sample
- Self-interstitial (Fe-Fe) $\langle 111 \rangle$ in a pure Fe sample
- Self-interstitial (Fe-Fe) $\langle 110 \rangle$ in a pure Fe sample
- Self-interstitial (Fe-Fe) $\langle 111 \rangle$ in a pure Cr sample
- Mixed interstitial (Fe-Cr) $\langle 110 \rangle$ in a pure Fe sample
- Mixed interstitial (Fe-Cr) $\langle 111 \rangle$ in a pure Fe sample
- Self-interstitial (Cr-Cr) $\langle 110 \rangle$ in a pure Cr sample
- Self-interstitial (Cr-Cr) $\langle 111 \rangle$ in a pure Cr sample
- Mixed interstitial (Fe-Cr) $\langle 110 \rangle$ in a pure Cr sample
- Mixed interstitial (Fe-Cr) $\langle 111 \rangle$ in a pure Cr sample

The benchmarking could only be performed at the endpoints of the Cr concentration diagram, since no other physically sound models for the Fe-Cr alloys could be found in literature.

The simulation samples were prepared by manually modifying the 1024 atom, perfect crystal samples of pure Fe and pure Cr. For the vacancy cases, this modification consisted of deleting the atom located at coordinates (0,0,0) in both samples. For the interstitial cases, these modifications consisted of adding an additional atom (atom 1025) to the end of the sample and shifting the first atom on the list (atom 1). The location of atom 1025 was determined by adding 0.5 \AA to the coordinates in the axes where the displacement was to occur, i.e., in x and y axes for $\langle 110 \rangle$ type interstitials and in all three axes for $\langle 111 \rangle$ type interstitials. The value of 0.5 \AA was subtracted from the respective coordinates of atom 1, therefore creating the relevant interstitial pair. The value of 0.5 \AA was determined by trial and error, as initial attempts to use a larger initial interstitial spacing (0.9 \AA) produced results in which the interstitial pair would fly apart during

energy minimization. For self-interstitials, an atom of the same type would be inserted into the sample, while the mixed interstitial samples received an atom of the opposite type.

The samples were then run, using LLNL's Multiprogrammatic Capability Cluster – MCR. This is a large (11.2 TF) tightly coupled Linux cluster with 1,152 nodes, each with two 2.4-GHz Pentium 4 Xeon processors and 4 GB of memory. MCR runs the LLNL CHAOS software environment, which incorporates the Red Hat Linux operating system [44]. The Molecular Dynamics (MD) code, Moldy [45], was set up for constant temperature of 0.01 K, no pressure, no chemical potential, with free sample volume, and a run of 3000 steps with a time step of 10^{-5} seconds. This number of steps was necessary in order to ensure that the sample had ample time to relax around the induced defect and that the final energy values converged. At the end of the run, the final total enthalpy values were extracted for each output and compared against those obtained from running the perfect crystal samples under the same conditions. The table listing the final values of total enthalpy for each sample is shown in Table 5.

Sample	Total Enthalpy [eV]
1024 Fe perfect crystal	-4221.373163
1024 Cr perfect crystal	-3928.353757
1023 Fe vacancy	-4215.461833
1023 Cr vacancy	-3921.989661
1025 self-interstitial <110> (Fe-Fe) in Iron	-4221.974874
1025 self-interstitial <110> (Fe-Fe) in Chromium	-3929.176430
1025 mixed interstitial <110> (Fe-Cr) in Iron	-4222.064124
1025 mixed interstitial <110> (Fe-Cr) in Chromium	-3928.756038
1025 self-interstitial <111> (Fe-Fe) in Iron	-4221.546602
1025 self-interstitial <111> (Fe-Fe) in Chromium	-3929.176430
1025 mixed interstitial <111> (Fe-Cr) in Iron	-4221.896441
1025 mixed interstitial <111> (Fe-Cr) in Chromium	-3928.756244
1025 self-interstitial <110> (Cr-Cr) in Chromium	-3926.664855
1025 self-interstitial <111> (Cr-Cr) in Chromium	-3926.579530

Table 5. Table of Final Values of Total Enthalpy for Pure Element Samples

The formation energies for the vacancy (E_{fv}) in pure elements are then computed from the total enthalpy of the pure element sample (E_{tot}^{1024}) and the total enthalpy of the sample with the vacancy (E_{tot}^{1023}), according to the following formula:

$$E_{fv} = E_{tot}^{1023} - 1023 \cdot \left(\frac{E_{tot}^{1024}}{1024} \right) \quad (14)$$

The formation energies for self interstitials (E_{fi}) were computed using a very similar approach, but incorporating the fact that samples which contain the interstitial consist of 1025 instead of 1023 atoms, and therefore correlating the energies in the following way:

$$EFI = E_{1025atoms}^{interstitial} - 1025 \cdot \left(\frac{E_{1024atoms}^{pure}}{1024} \right), \quad (15)$$

where $E_{1025atoms}^{interstitial}$ is the total enthalpy of the sample with 1025 atoms and a self interstitial and $E_{1024atoms}^{pure}$ is the total enthalpy of the sample with the pure element in pure crystal 1024 atom arrangement.

For the mixed interstitial samples, however, a different methodology must be applied, defining the formation energy of the interstitial as follows:

$$EFI = E_{1025atoms}^{1Cr interstitial} - E_{reference} \quad (16)$$

where

$$E_{reference} = E_{interpolation} + E_{from-hof}$$

and

$$E_{interpolation} = n_{Cr} \cdot E_{peratom}^{pureCr} + n_{Fe} \cdot E_{peratom}^{pureFe}$$

$E_{from-hof}$, however, is a product of a polynomial fit to Δh [eV/atom] as seen in figure 3-4, and as we are working in the region below 6 % of Cr concentration, where this difference function is negative, we must only use the Δh values from a series of samples with an increasing Cr concentration, relaxed by running them through the Moldy code, as seen below:

xCr	$\Delta h[\text{eV/atom}]$
0	0
0.00097	-9.65E-05
0.006836	-0.000564056
0.012695	-0.000492174
0.015625	-0.000884431
0.019531	-0.001196044
0.030273	-0.000627474
0.038086	-0.000667051
0.047852	1.16076E-05

Table 6. Values of $\Delta h[\text{eV/atom}]$ as Obtained by Modeling

When fitted with a 4th order polynomial using Excel, this produces the following heat of formation function in the sub-6% Cr concentration region:

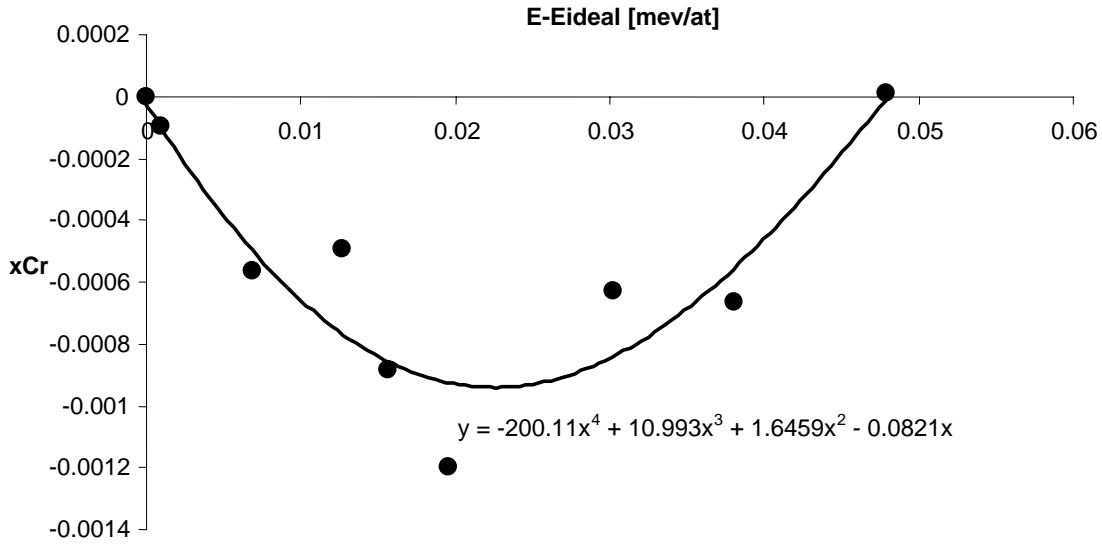


Figure 21. Heat of Formation Fit Below 6% Cr concentration

Therefore, when x is calculated as the value of $x = 1/1025$ and the corresponding y turns out to be -7.85209×10^{-05} meV/atom. $E_{from-hof}$ is the 1025th multiple of that value of y and is then entered into (16).

The results of this characterization are displayed in Table 7.

Self Interstitial (Cr-Cr) <111> Energy of Formation	-
Self Interstitial (Cr-Cr) <110> Energy of Formation	-
Mixed Interstitial (Fe-Cr) <111> Energy of Formation	3.61
Mixed Interstitial (Fe-Cr) <110> Energy of Formation	3.43
Self Interstitial (Fe-Fe) <111> Energy of Formation	3.95
Self Interstitial (Fe-Fe) <110> Energy of Formation	3.52
Vacancy Energy of Formation	1.72
Element	
Fe	
Cr	

Table 7. Formation Energies for the Pure Element Characterization

C. EVALUATING THE VACANCY ENERGY OF FORMATION

In order to analyze the effect of increased Cr concentration on the formation energy of a single vacancy, it was necessary to characterize this behavior with a series of samples of increasing Cr concentration. Also, since it is unknown what the influence of the distance between the solute Cr atoms and the vacancy is, it was necessary to analyze the entire ensemble of possible configurations.

Therefore, 11 samples of 1024 atoms with Cr concentrations ranging from a singular Cr atom to 17 % were simulated using the molecular dynamics code Moldy [45], and set up for a constant temperature of 0.01 K, no pressure, no chemical potential, with free sample volume, and a run of 3000 steps with a time step of 10^{-5} seconds. These runs provided the reference values of total enthalpy for the pure crystal samples. Those values are shown in Table 8.

Cr Concentration	Total Enthalpy [eV]
9.77E-04	-4221.45017
0.01563	-4221.88415
0.03027	-4221.0655
0.04785	-4219.7705
0.06055	-4217.80019
0.07422	-4214.18631
0.08984	-4210.24463
0.09668	-4209.23258
0.10645	-4206.00442
0.11523	-4203.40938
0.17188	-4184.4663

Table 8. Total Enthalpy of the reference samples

Thereafter, each of the samples was run through a sequence of two programs using a LINUX script. The first program went through the sample and removed one atom at a time, creating a vacancy. Only Fe atoms were removed in order to maintain the Cr composition. At the end of operation, approximately 1000 vacancy samples were ready, representing all possible configurations. Next, all of the newly created samples were simulated using the molecular dynamics code Moldy, and set up for a constant temperature of 0.01 K, no pressure, no chemical potential, with free sample volume, and a run of 3000 steps with a time step of 10^{-5} seconds. In the end, the LINUX code extracted the final values of total enthalpy from each sample output file.

A histogram of energies could then be produced for each set of samples containing the same number of Cr atoms. Over this histogram, a Gaussian distribution function was fitted using ORIGINTM with the canonical form of

$$y = y_0 + \frac{A}{w\sqrt{\frac{\pi}{2}}} \cdot e^{-2\left(\frac{x-x_c}{w}\right)^2} \quad (17)$$

where y_0 , A , x_c and w are fitting parameters. In our case, x_c provides us with the mean value of the total enthalpy of the sample and w provides us with the width of the 2/3 width of the Gaussian, which represents one standard deviation of results and gives us the width of the error bars. Each mean value for total enthalpy of a sample including a vacancy was then used in conjunction with the respective value of total enthalpy of the perfect crystal to provide the formation energy of the vacancy at the given Cr concentration. Since this equation is first-order linear, the uncertainty in E_{tot}^{1023} , as obtained from the Gaussian fit (w), transfers directly into E_{fv} . The vacancy formation energies obtained are shown in Table 9.

Cr Concentration	Vacancy Energy of Formation (eV)	w/2
9.77E-04	-1.713903803	0.00215
0.01563	-1.715881926	0.0749
0.03027	-1.71444999	0.01249
0.04785	-1.722512512	0.01765
0.06055	-1.761504721	0.05799
0.07422	-421414418.6	0.06145
0.08984	-1.785316452	0.06531
0.09668	-1.799338475	0.06517
0.10645	-1.838959668	0.06851
0.11523	-1.812067625	0.06319
0.17188	-1.863116579	0.05324

Table 9. Vacancy Formation Energy as a Function of Cr Concentration

D. OBTAINING THE FORMATION ENERGIES OF INTERSTITIALS

The procedure for obtaining the formation energies of self-interstitials is quite analogous to those described for the evolution of vacancy formation energy and for self-interstitial cases in the pure elements. After obtaining the reference values for the samples in the perfect crystal state, the samples are operated on by a program which places an interstitial atom added at each and every atom site containing a Fe atom. The program

displaces the original atom by 0.5 \AA away from its original location and adds its mirror image atom. The displacement takes place in x and y axes for interstitials $\langle 110 \rangle$ and all three axes for interstitials $\langle 111 \rangle$. After creating approximately 1000 samples for each Cr concentration examined, the script then runs each of them in a Moldy code, with the inputs set at a constant temperature of 0.01 K, no pressure, no chemical potential, with free sample volume, and a run of 3000 steps with a time step of 10^{-5} seconds. The extracted values of final enthalpy are then sorted in an energy histogram and a Gaussian fit is applied, thus providing us with the mean energy value for each selected concentration as well as an indication of uncertainty based on the configurational characteristics of the sample. The values of final enthalpy for pure crystal samples, median values for those containing an interstitial, their individual uncertainties and the self-interstitial formation energy calculated via equation (15) are shown in Table 10.

Cr Concentration	Formation Energy $\langle 110 \rangle$ eV	w/2 $\langle 110 \rangle$	Formation Energy $\langle 111 \rangle$ eV	w/2 $\langle 111 \rangle$
0.000976	3.519643423	0.004155	3.942243423	0.00729
0.006829	3.516942656	0.006155	3.941462656	0.00883
0.012683	3.512976597	0.019815	3.932626597	0.014195
0.030244	3.506226279	0.031625	3.911206279	0.020885
0.047805	3.504111963	0.04858	3.844751963	0.07725
0.074146	3.494965576	0.106945	3.811195576	0.06379
0.106341	3.498952173	0.154455	-	-
0.12	3.48620728	0.171505	-	-
0.145366	3.47881083	0.19146	-	-
0.171707	3.47969771	0.19536	-	-

Table 10. Energetics of Self-Interstitial Samples

To obtain the evolution of mixed interstitial formation energies, we apply an almost exact procedure, except that when inserting an atom we are introducing a Cr, rather than a Fe. As this changes the global composition of the sample, we must correct for this using equations (16). In order to obtain $E_{\text{from hof}}$ value it is necessary to make a dual zone polynomial fit. In this case zone A is below 6% Cr concentration and zone B

covers the area between 6-20% Cr concentrations. The relevant equations and fits are shown in Figures 22 and 23.

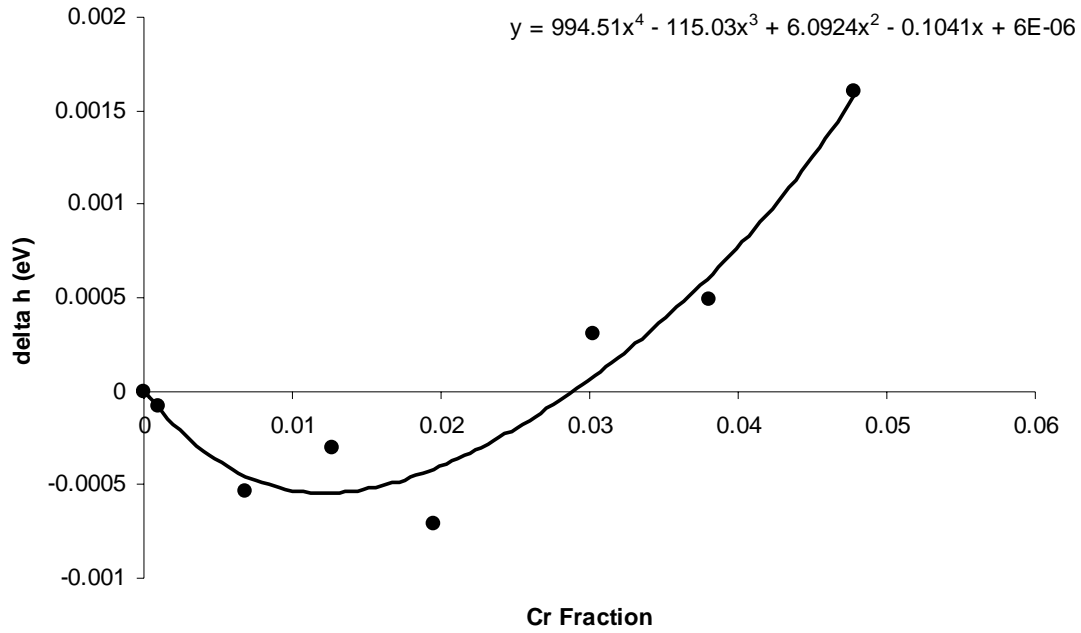


Figure 22. Polynomial Fit in the sub 6% Cr Concentration Eegion

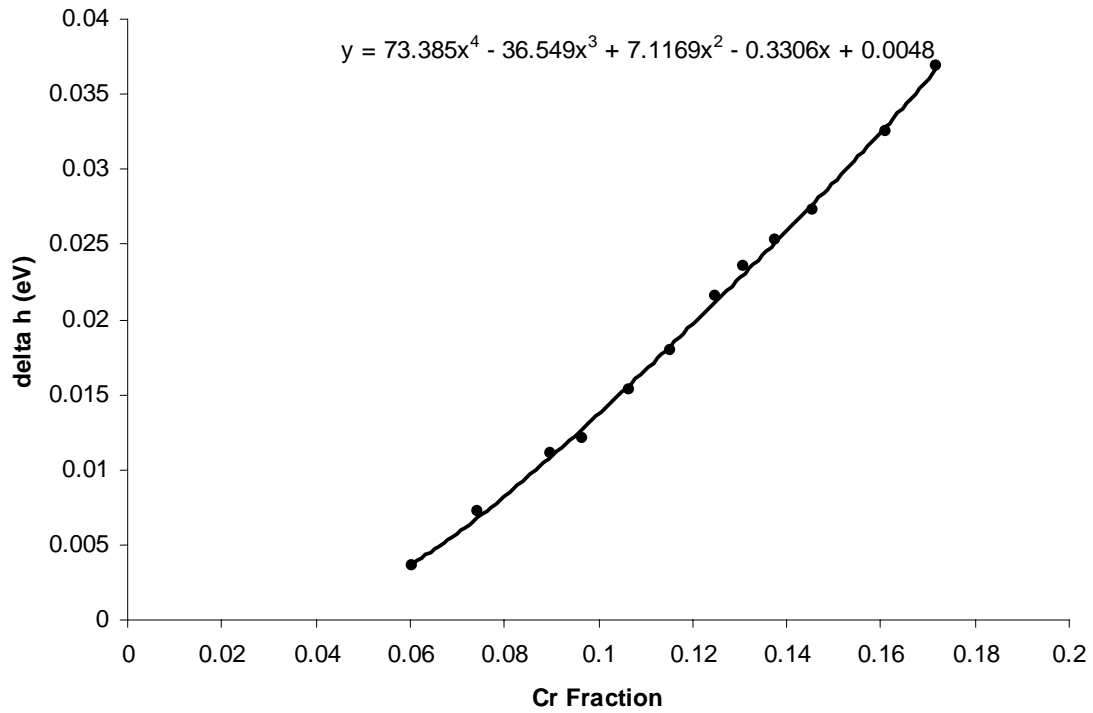


Figure 23. Polynomial Fit to the 6-20 % Region of Cr Concentration

The resulting energetics of mixed interstitials are shown below in Table 11:

Cr Concentration	Formation Energy <110> eV	w/2 <110>	Formation Energy <111> eV	w/2 <111>
0.001951	3.428325907	0.007	3.596965907	0.004155
0.007805	3.433025476	0.01334	3.591255476	0.021995
0.013659	3.432935366	0.0165	3.603105366	0.033825
0.03122	3.467658628	0.06466	3.608058628	0.062045
0.04878	3.509552851	0.0963	3.628022851	0.12394
0.075122	3.550068635	0.105995	3.633258635	0.15496
0.107317	3.546490688	0.10822	3.621460688	0.184035
0.120976	3.537463852	0.109665	3.604573852	0.192875
0.146341	3.530354706	0.126305	3.546284706	0.140005
0.172683	3.484627439	0.124385	3.501687439	0.18874

Table 11. Mixed Interstitial Energetics in eV

THIS PAGE INTENTIONALLY LEFT BLANK

VI. ANALYSIS AND CONCLUSION

A. VACANCIES

As we can see from Figure 24, our results for vacancy formation energy in Fe are lower than DFT calculations.. However, when we consider the fact that most of these calculations were either thermally unequilibrated (unrelaxed) or had a volume constraint, this becomes a much more believable result. Both of these conditions led to additional “frustration” within the sample, and accordingly to a higher formational enthalpy. References for all values quoted are listed at the end of the chapter.

On the other hand, when we compare the vacancy formation energy in Cr with other results (Figure 25), as well as those calculations which produce both results (Figure 26), we see that it falls neatly in between *ab initio* and other classical results. From both of these comparisons we can conclude that our potential gives a reasonable prediction of vacancy formation energies for both pure elements, as well as for their mutual relationship.

The more extensive analysis of vacancy formation energy behavior as a function of Cr concentration yields some fascinating results. Prior to this work it has been supposed that the vacancy formation energy would follow a direct interpolation between the pure element values. As we can see in Figure 27, the true formation energy deviates from the assumed linear interpolation in Figure 26 in the region below 6% Cr concentration, which is the same region in which the heat of formation curve shows the same deviant behavior from linear interpolation. In real terms, this finding means that it is more likely for vacancies to form in alloys with a Cr concentration smaller than 6%, than those above this value. The exact nature of this effect on the physical properties of the alloy is as of now undeterminable; however, it can be hypothesized that it will be observable. Additionally, the increasing spread of values as a function of Cr concentration shows a strong interactivity between the impurities and vacancies.

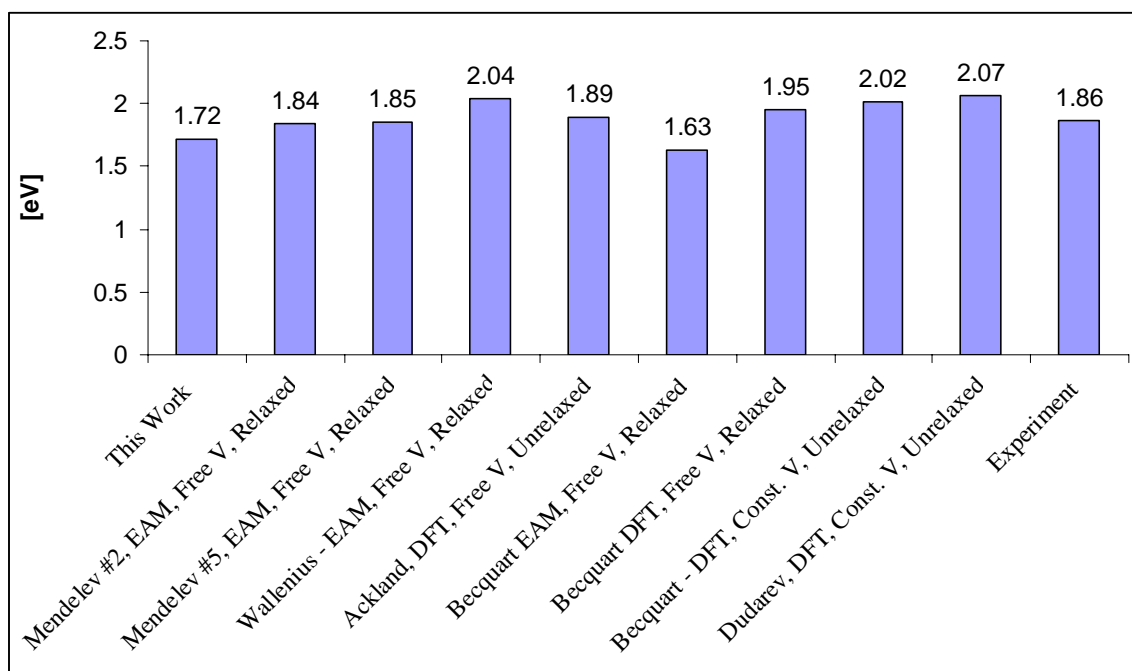


Figure 24. Vacancy Formation Energies in Iron

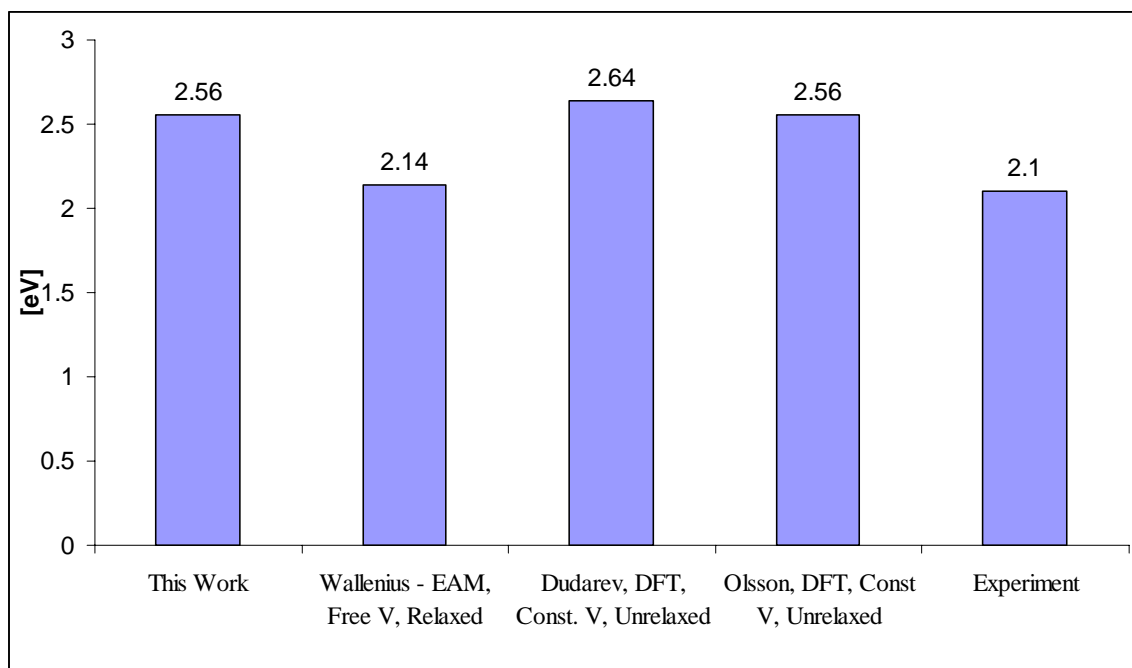


Figure 25. Vacancy Formation Energies in Chromium

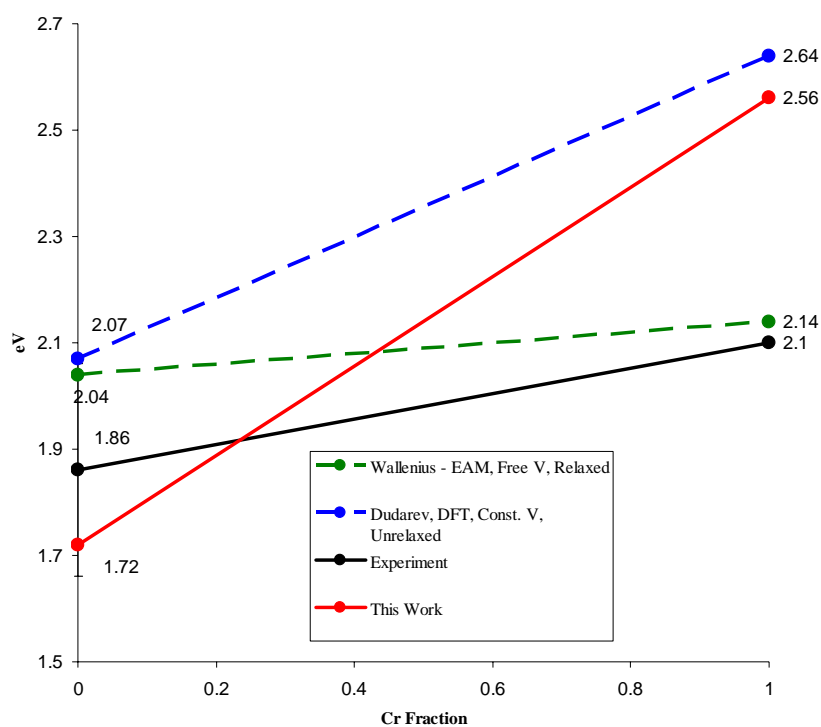


Figure 26. Linear Interpolation Between EFV in Fe and Cr

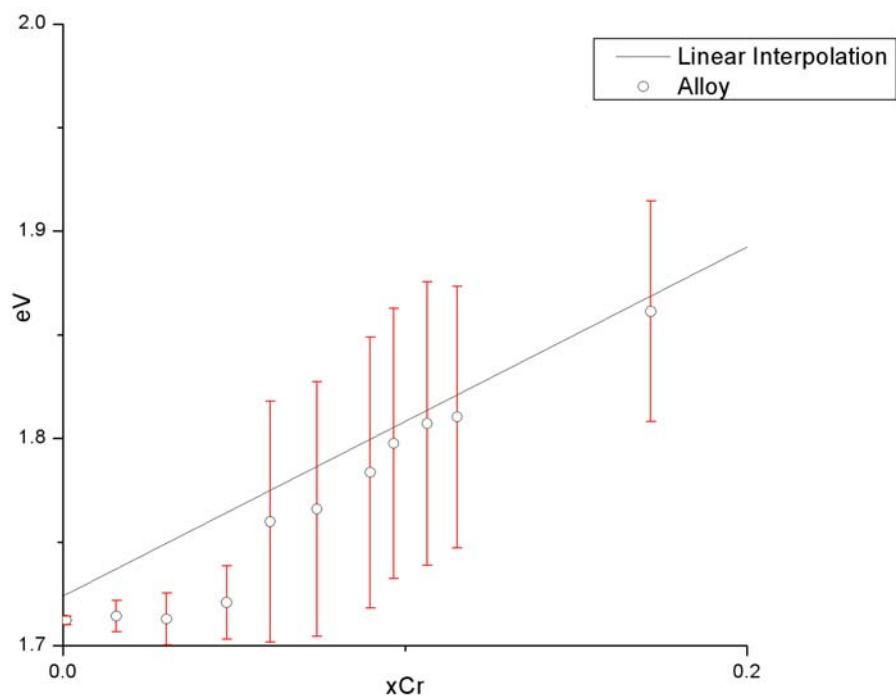


Figure 27. Evolution of Vacancy Formation Energy as a Function of Cr

B. SELF-INTERSTITIALS

As we can see from Figures 28 and 29 our results match both the relative order and the magnitude of target *ab initio* calculations. The critical part of this fitting was achieving the same relative order of values for mixed and self interstitials in iron, as both theory and experiment suggest the mixed interstitial to be the prime defect in Fe-Cr alloys [45].

Examining the plot of interstitial formation energy as a function of Cr concentration yields some exceptionally interesting information. While the formation energy of the interstitial in $\langle 110 \rangle$ remains relatively stable around 3.5 eV per defect, and actually drops lower as Cr concentration increases, the $\langle 111 \rangle$ curve shows some highly unstable behavior. An initial examination of energy histograms, produced by compiling and sorting the final output enthalpies of all samples initialized with a $\langle 111 \rangle$ interstitial, showed a behavior that deviated significantly from that which was expected. For example, Figure 30 shows the energy histogram for samples containing 10.6 % Cr atoms and an interstitial in $\langle 110 \rangle$. The energies in the histogram follow a normal distribution which can be approximated and analyzed with a Gaussian curve fit as overlaid. For samples which contain just a single Cr atom the values are also normally distributed (see Figure 31); however, their variance is much smaller because most configurations interact equally with the interstitial. The only deviants are those where the Cr atom is in the near neighborhood of the interstitial site.

However, when we take a look to the histogram of sample enthalpies with 0.006 Chromium concentration, in Figure 32, we make the astonishing observation that there is not one, but two distinct distributions of energies. Upon closer examination, we notice that the larger distribution has a mean value which is equivalent to that of the distribution for samples with the $\langle 110 \rangle$ interstitial at the same Cr concentration. This inevitably leads us to conclude that a number of samples, even though initially seeded with a $\langle 111 \rangle$ interstitial, converted to an interstitial in the $\langle 110 \rangle$ direction during the process of energy minimization. Physically, this means that the $\langle 111 \rangle$ interstitial is not a preferred state for the defect and even if induced it will tend to convert into a $\langle 110 \rangle$ type interstitial. The fraction of samples which convert into a $\langle 110 \rangle$ type interstitial increases steadily as shown in Figure 33. This increase, combined with the fact that the differential between

self-interstitial formation energies in $\langle 110 \rangle$ and $\langle 111 \rangle$ decreases as seen in Figure 34, makes it impossible to discern the existence of a peak with final enthalpies for samples containing the $\langle 111 \rangle$ type interstitial after approximately 10 % because the variance has increased so much that the two distributions completely overlap.

C. MIXED INTERSTITIALS

When looking at the mixed interstitials and their formation energy evolution as a function of Cr concentration, we note several important differences when compared to the self-interstitials.

In this case, it is the $\langle 110 \rangle$ interstitial that has a lower energy of formation, therefore being the preferable state. However, both mixed interstitial curves, as can be inferred from comparing Figure 35 with Figure 34, are above those for self-interstitials. However, they are both exceptionally stable and well behaved, so much so that they run almost parallel above 10 % in concentration and even have very little overlap when their variances are taken into account.

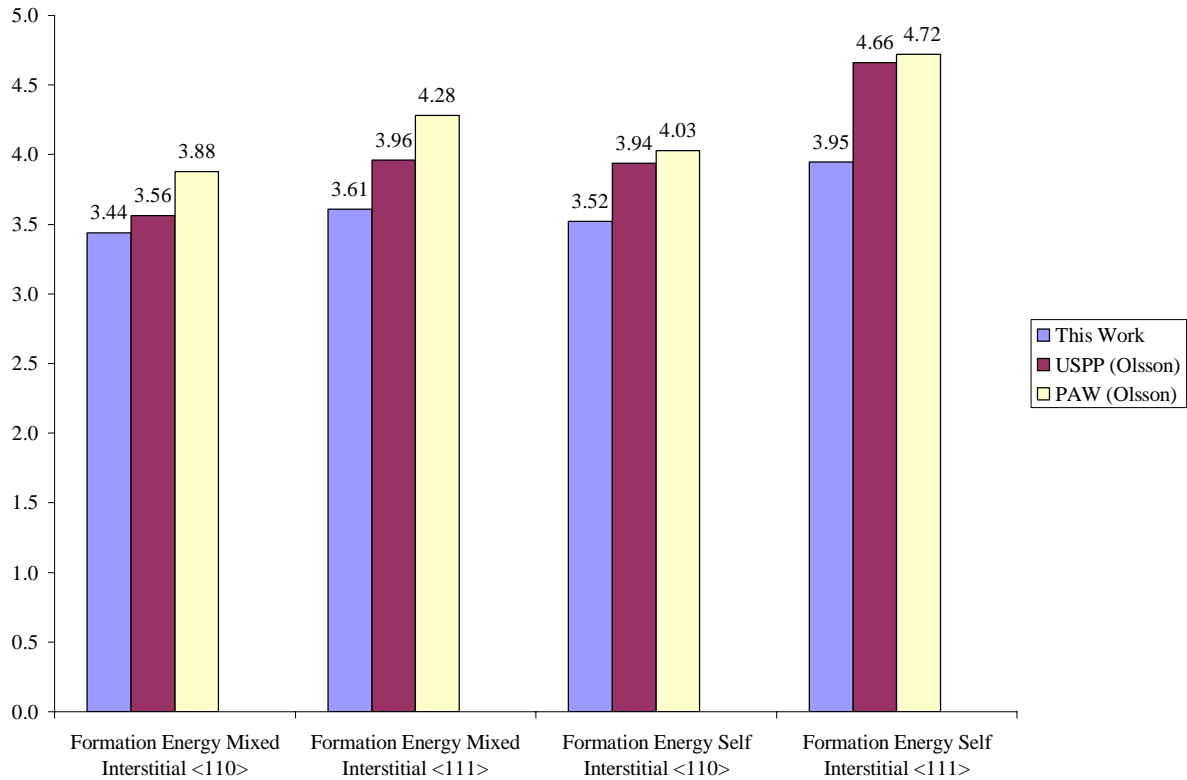


Figure 28. Formation Energies for Interstitials in Iron [45]

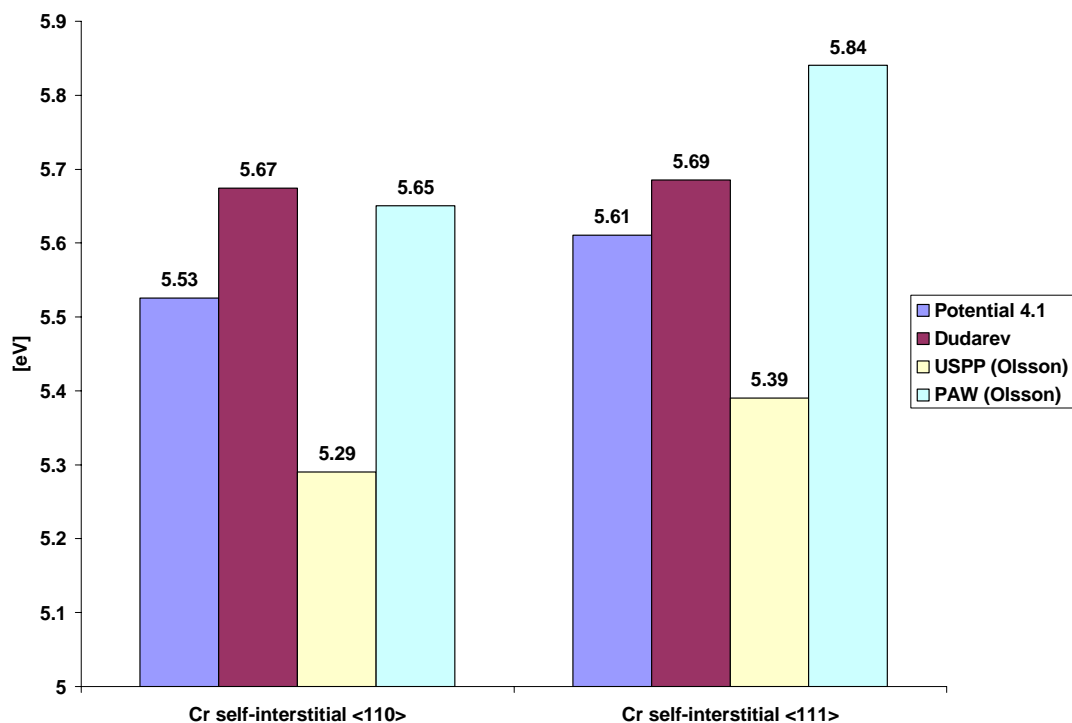


Figure 29. Formation Energies for Self-Interstitials in Chromium

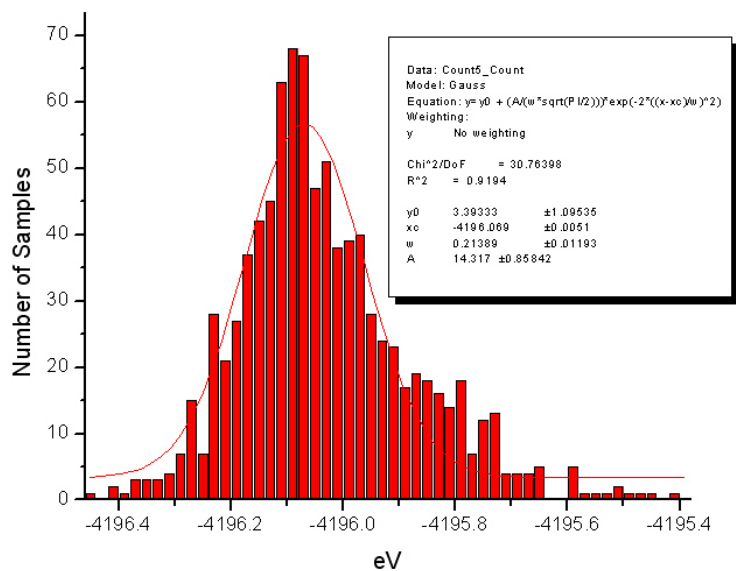


Figure 30. Energy Histogram for Self-Interstitial Samples in the <110> direction at higher Cr Concentration

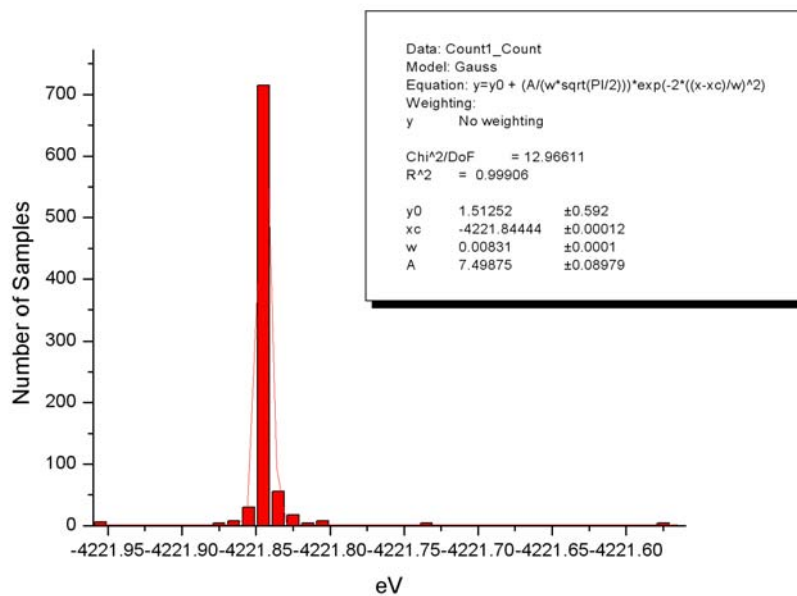


Figure 31. Histogram of Energies for Self-Interstitial Samples in the <110> direction at lower Cr Concentration

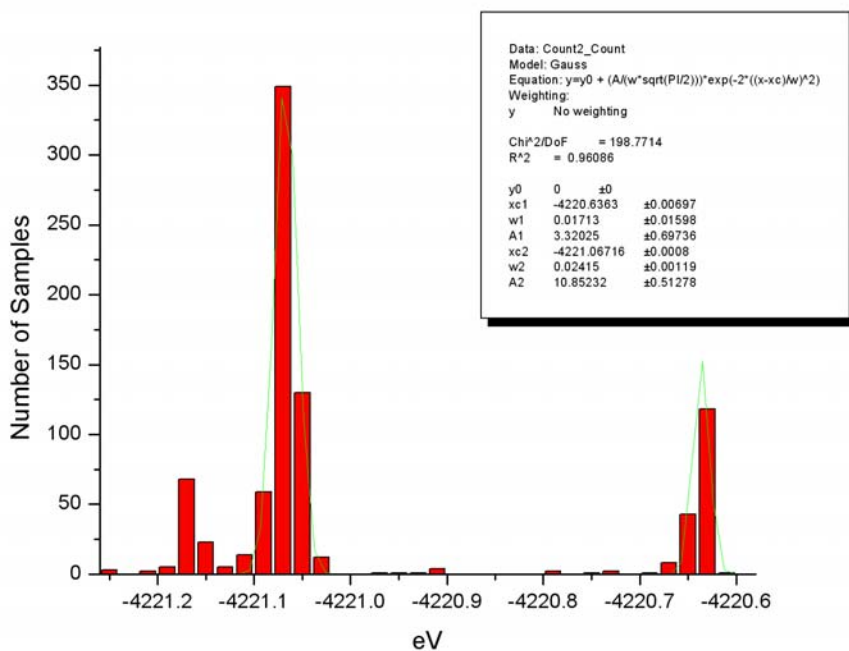


Figure 32. Histogram of Energies for Self-Interstitial Samples in <111>

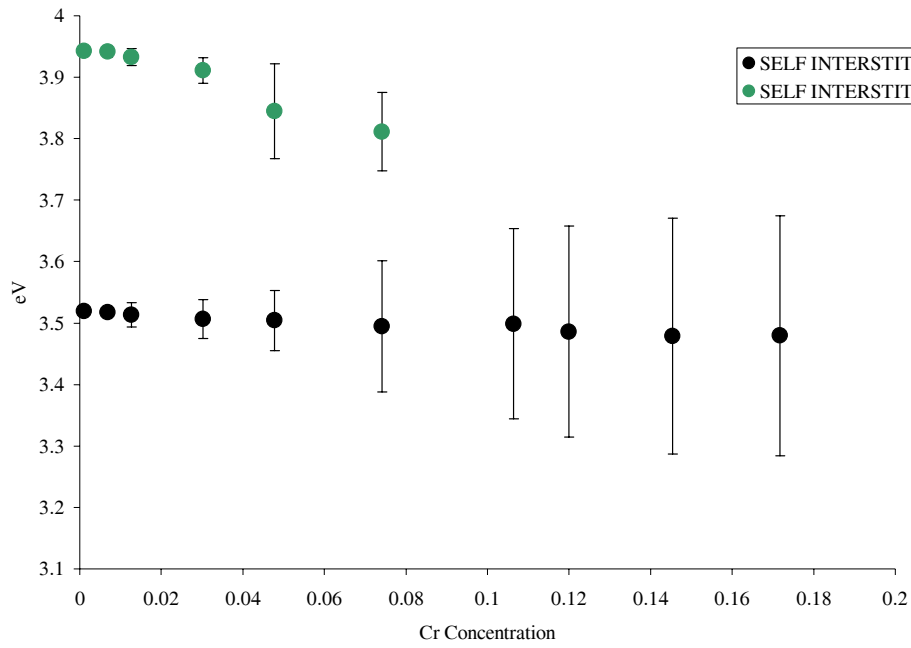


Figure 33. Evolution Self-Interstitial Formation Energies

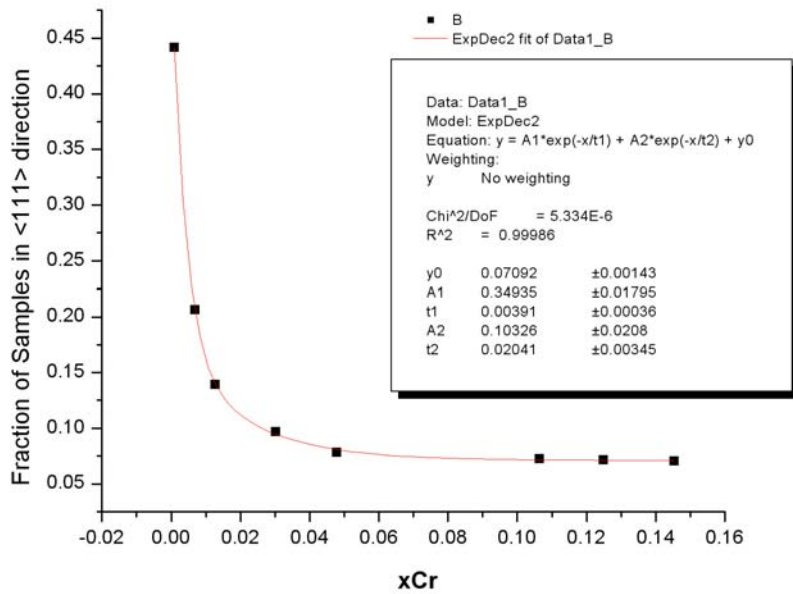


Figure 34. Partition Function for Stability of Self –Interstitial in <111>

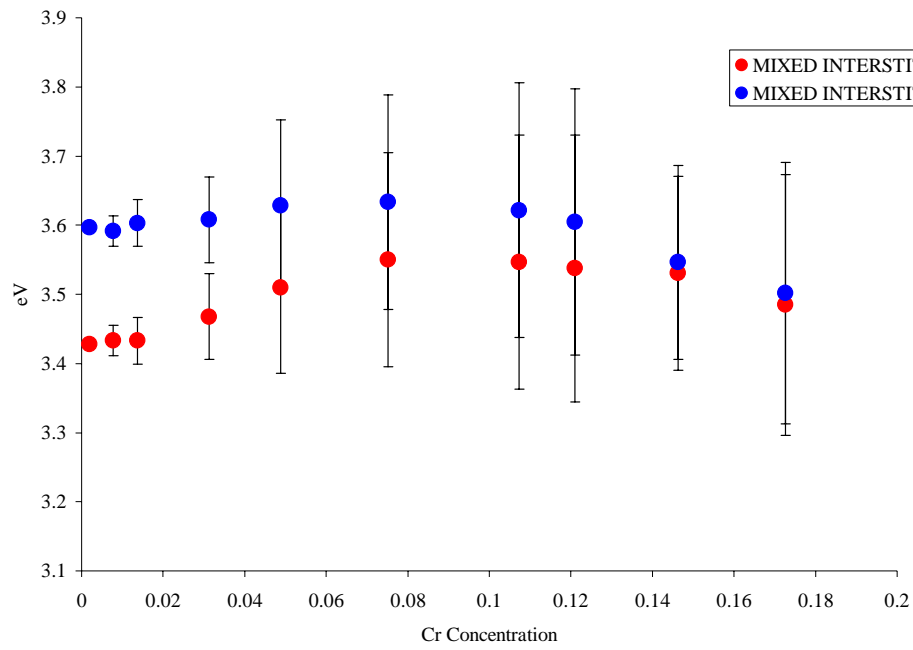


Figure 35. Evolution of Mixed-Interstitial Formation Energies

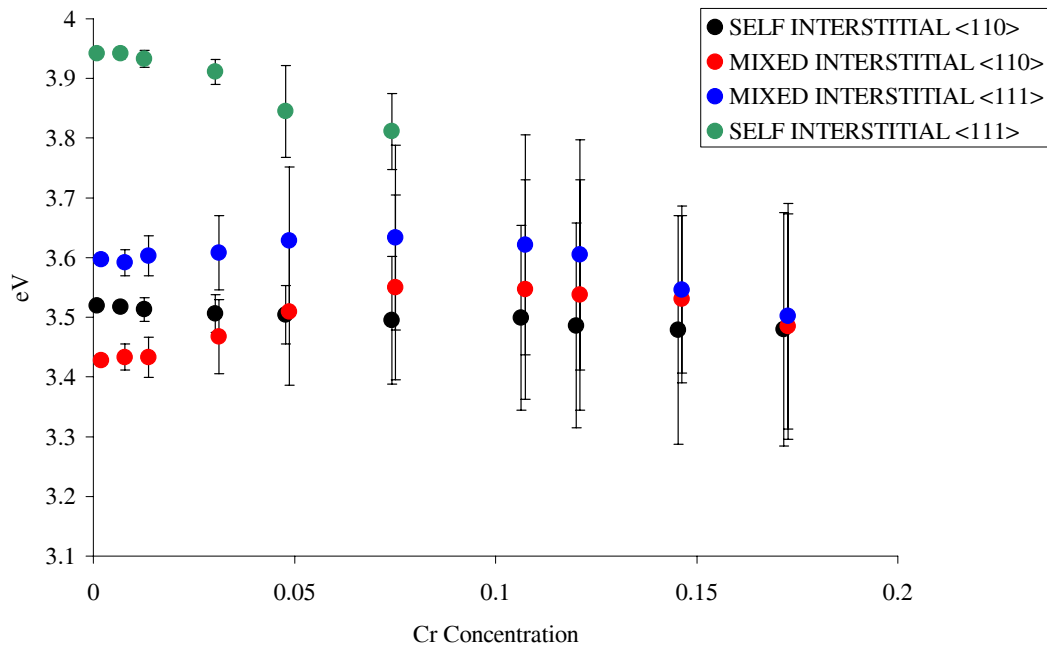


Figure 36. Combined Interstitial Evolution Plot

D. CONCLUSIONS

If we look at Figure 36, we can see that all interstitial types behave in a very similar manner higher the Cr concentration. It is not clear what physical significance this prediction could have, but it would have to be validated through either experimental methods or *ab initio* calculations, before further discussion can ensue. Nonetheless, the ability of EAM to offer such thorough evaluations should be noted.

To conclude, it has been proven that this methodology [29] adequately approximates results obtained through *ab initio* calculations. It has also been demonstrated that by using this methodology, the studies of point defects can be of a larger scale and more exhaustive than is the case with the currently available *ab initio* models.

The results produced in this research will go into studies of dynamic properties of point defects such as vacancy migration and defect clustering. In the meantime, though, a interim step is a study of precipitation properties of Fe-Cr alloys, which will have a high fidelity considering that the underlying assumptions, i.e., the interatomic potentials, have already been validated as providing an accurate approximation of *ab initio* results, and by inference real world physical behavior.

In order to study this behavior, a hybrid Monte Carlo-molecular dynamics code named MCCASK was developed by A. Caro and B. Sadigh in 2005 at Lawrence Livermore National Laboratory. The code performs sequences of Monte Carlo events and Molecular Dynamics time steps. In this way, the equilibrium concentrations in the alloy are obtained.

The molecular dynamics part of the MCCASK code is based in MDCASK, a molecular dynamics code that was first developed to study radiation damage in metals. MDCASK solves the equation of motion of the atoms in the sample; energy and forces on each atom are calculated using an interatomic potential, and the equations of motion are integrated to obtain the next values of positions and velocities. The Monte Carlo part of the new code MCCASK corresponds to a parallel MC code in the transmutation ensemble (T,P,N,Dm), with N the total number of atoms and Dm the difference in chemical potential [46].

Computational materials science is a young field, which has just recently been handed the tools of its trade--high-end computing hardware and software--and over the coming years it is inevitable that major advances in modeling will result in real life impact, not only in the field of nuclear energy, but in everyday applications. The future is bright.

THIS PAGE INTENTIONALLY LEFT BLANK

VII. SUMMARY OF RESEARCH

In summary, it can be said that the suitability of Fe-Cr alloys for use in cladding, wrappers and in-core structural components in Generation IV advanced nuclear systems necessitates a thorough understanding of their behavior under irradiation, to include formation energies of point defects such as vacancies and interstitials in the steel matrix. This work used a powerful methodology developed by A. Caro, et al. [29] to determine the energetics of vacancies and interstitials both in pure elements and as a function of Cr concentration. An overview of the methodology is shown in Figure 37.

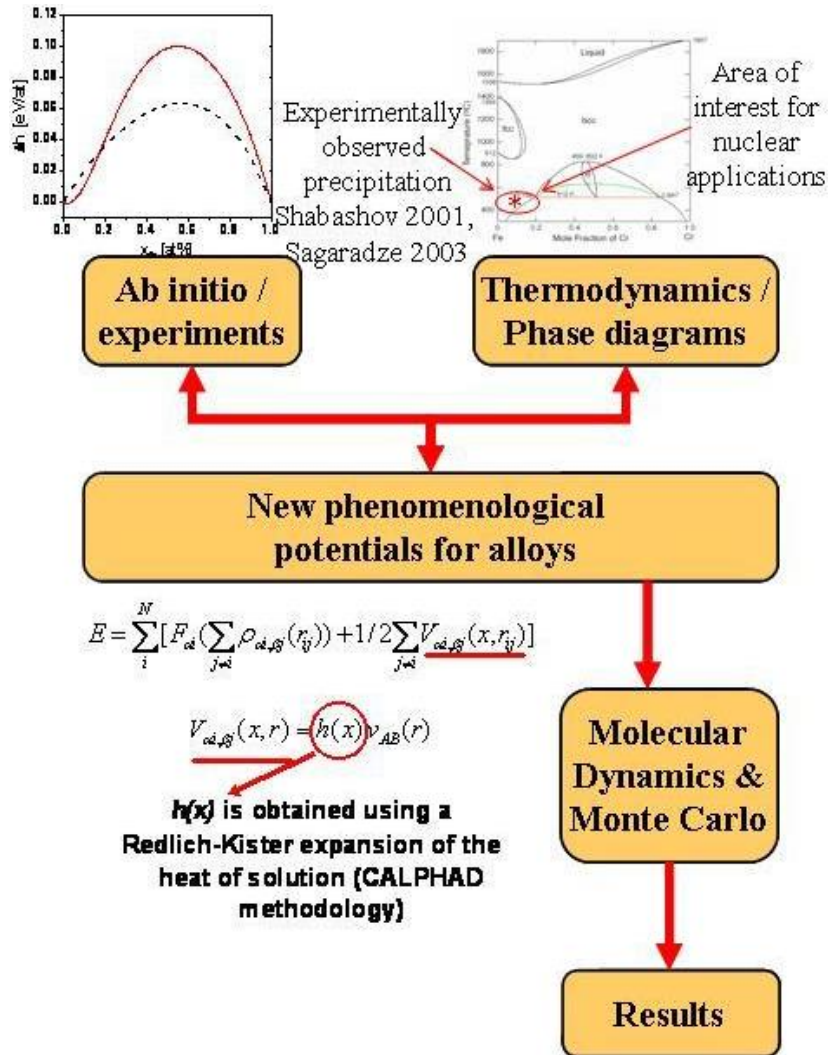


Figure 37. Research Methodology [29]

Results of this research proved that the methodology is appropriate and can be utilized for large scale simulation, and that it approximates *ab initio* results satisfactorily. In addition to that, the evaluation of point defect formation energy as a function of Cr concentration, gave some interesting predictions concerning their static properties and stability. A finding relating the stability of the $\langle 111 \rangle$ Fe self-interstitial to local Cr concentration is summarized in Figure 38.

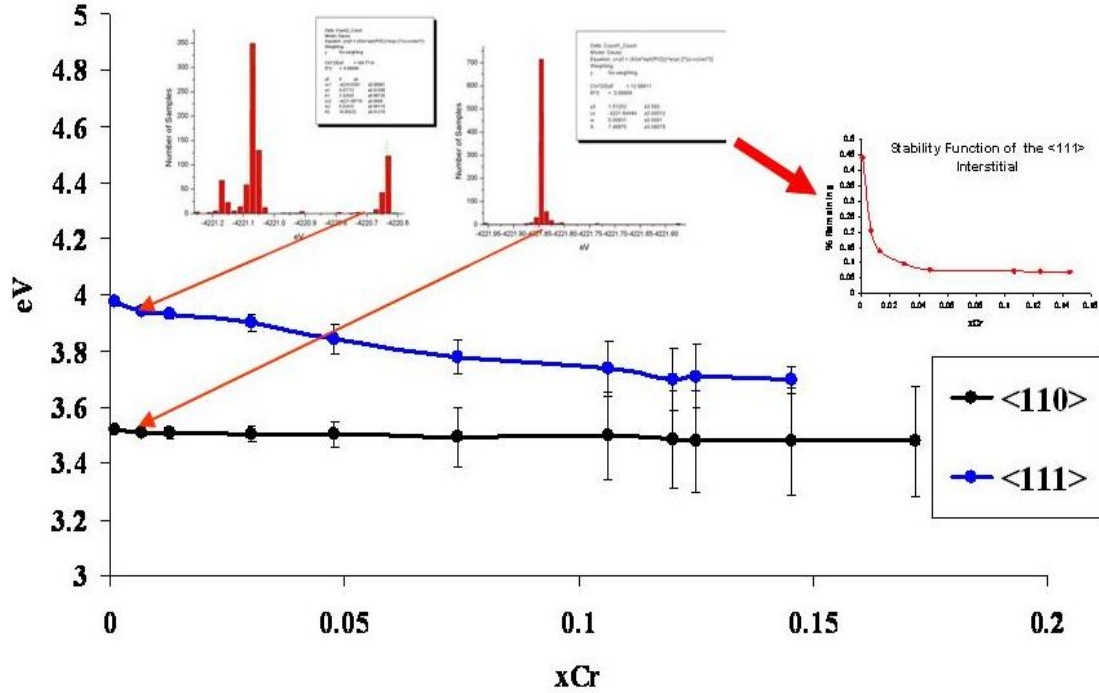


Figure 38. Development of the Stability Function for Fe Self-interstitial in $\langle 110 \rangle$

We can therefore say that the results obtained in this thesis can be used for studies of dynamic properties and time evolution of point defects. The stability predictions will need to be verified through *ab initio* or experimental data, but at the very least they can serve to demonstrate the potential benefits of using molecular dynamics and semi-empirical potentials to approximate first principles calculations.

LIST OF REFERENCES

- [1] L. Badash, E. Hodes, A. Tiddens, *Nuclear Fission: Reaction to the Discovery in 1939*, Institute on Global Conflict and Cooperation, UC San Diego, San Diego, 1985
- [2] Retrieved from <http://www.atomicarchive.com/History/firstpile/index.shtml>
- [3] Retrieved from http://www.anl.gov/Science_and_Technology/History/Anniversary_Frontiers/10photo.html
- [4] J.R. Lamarsh, A.J. Baratta, *Introduction to Nuclear Engineering*, 3rd edition, pp. 87, Prentice Hall, Upper Saddle River, New Jersey, 2001
- [5] Retrieved from <http://www.uic.com.au/uicphys.htm>
- [6] Idaho National Laboratory, *Generation IV Nuclear Energy Systems Ten-Year Program Plan, Volume 1*, pp. 2, U.S. Department of Energy, Office of Nuclear Energy, July 2006
- [7] Summarized from <http://www.uic.com.au/nip16.htm>
- [8] Generation IV International Forum, *A Technology Roadmap for Generation IV Nuclear Energy Systems*, U.S. Department of Energy, Nuclear Energy Research Advisory Committee, December 2002.
- [9] Retrieved from <http://www.gnep.energy.gov/gnepAdvancedBurnerReactors.html>
- [10] Retrieved from <http://gen-iv.ne.doe.gov/>
- [11] Idaho National Laboratory, *Generation IV Nuclear Energy Systems Ten-Year Program Plan, Volume 2: Appendices, Appendix 4.0*, U.S. Department of Energy, Office of Nuclear Energy, July 2006
- [12] J.R. Lamarsh, A.J. Baratta, *Introduction to Nuclear Engineering*, 3rd edition, pp. 119, Prentice Hall, Upper Saddle River, New Jersey, 2001
- [13] Retrieved from <http://gen-iv.ne.doe.gov/Fast-SpectrumReactors.asp>
- [14] Hecht, Jeff. *U.S. Plans Portable Nuclear Power Plants*, New Scientist, 03 September 2003
- [15] D. S. Billington, J.H. Crawford, *Radiation Damage in Solids*, pp. 56, Princeton University Press, Princeton, New Jersey, 1961.
- [16] Retrieved from <http://www.siliconfareast.com/crystaldefects.htm>

- [17] C. Domain, C.S. Becquart. *Phys. Rev. B* **65**, 024103, 2002
- [18] G.R. Odette, G.E. **Lucas**. *JOM*, **53** (7), pp. 18-22, 2001
- [19] S.J. Zinkle, Y. Matsukawa. *JOM*, 329–333, 2004
- [20] Retrieved from <http://fti.neep.wisc.edu/neep423/FALL97/lecture42.pdf#search=%22displacement%20per%20atom%22>
- [21] Retrieved from <http://www.cmpgroup.ameslab.gov/cmsn/otherlinks/ssi/atomistic.html>
- [22] Retrieved from http://iron.nuc.berkeley.edu/~bdwirth/Public/NE220/documents/Section7_06.pdf.
- [23] Retrieved from http://eed.llnl.gov/nuclear_workshop/presentations/Session%202E/Zinkle/materialsmodelingsjz.pdf
- [24] Retrieved from http://www.asm-easternny.org/docs/2004symp/3-1_Zinkle.pdf#search=%22Oak%20ridge%20materials%20Zinkle%20NASA%20Space%20reactor%22
- [25] Idaho National Laboratory, *Generation IV Nuclear Energy Systems Ten-Year Program Plan, Volume 2: Appendices, Appendix 9.0*, U.S. Department of Energy, Office of Nuclear Energy, July 2006
- [26] Personal Communication with Dr. M. Serrano de Caro, LLNL
- [27] B.D. Wirth, G.R. Odette, J. Marian, L. Ventelon, J.A. Young-Vandersall, L.A. Zapeda-Ruiz. *Journal of Nuclear Materials* 329–333, pp. 103-111, 2004
- [28] Retrieved from <http://iron.nuc.berkeley.edu/%7Ebdwirth/Public/WRG/wrg.html>
- [29] A. Caro, D. Crawson, M. Caro *PRL* **95** 12 Aug 2005
- [30] M. S. Daw, S.M. Foiles, and M. I. Baskes, *Mater. Sci. Rep.* **9**, 251, 1993.
- [31] G. J. Ackland and V. Vitek, *Phys. Rev. B* **41**, 10 324, 1990.
- [32] M. I. Baskes, *Phys. Rev. B* **46**, 2727, 1992.
- [33] E. O. Arregui, M. Caro, and A. Caro, *Phys. Rev. B* **66**, 054201 (2002).
- [34] A. Caro, P. E. A. Turchi, M. Caro, and E. M. Lopasso, *J. Nucl. Mater.* **336**, 233, 2005.
- [35] P. Olsson, I. A. Abrikosov, L. Vitos, and J. Wallenius, *J. Nucl. Mater.* **321**, 84, 2003.

- [36] M. I. Mendelev, S. Han, D. J. Srolovitz, G. J. Ackland, D.Y. Sun, and M. Asta, *Phil. Mag.* **83**, 3977, 2003.
- [37] J. Wallenius, P. Olsson, C. Lagerstedt, N. Sandberg, R. Chakarova, and V. Pontikis, *Phys. Rev. B* **69**, 094103, 2004.
- [38] N. Saunders and A. P. Miodownik, *CALPHAD: A Comprehensive Guide*, edited by R.W. Cahn, Pergamon Materials Series, Oxford, New York, 1998.
- [39] Tables with the potential are available upon request to the author, subject to approval by Dr. A. Caro.
- [40] I. Mirebeau, M. Hennion, and G. Parette, *Phys. Rev. Lett.* **53**, 687, 1984.
- [41] M. Hennion, *J. Phys. F* **13**, 2351, 1983.
- [42] K. Ohno, K. Esfarjani, Y. Kawazoe. *Computational Materials Science: From Ab Initio to Monte Carlo Methods*, pp. 285-286 Springer-Verlag, Berlin Heidelberg, Germany, 1999
- [43] M.P. Allen and D.J. Tildeseley, *Computer Simulation of Liquids* Clarendon, Oxford, 1989.
- [44] Retrieved from <http://www.llnl.gov/linux/mcr/>
- [45] P. Olsson, I.A. Abrikosov, L. Vitos and J. Wallenius. *J. Nucl. Mater.* 321, pp. 84-90, 2003
- [46] Retrieved from <http://www.llnl.gov/asci/purple/benchmarks/limited/mdcask/>

THIS PAGE INTENTIONALLY LEFT BLANK

INITIAL DISTRIBUTION LIST

1. Defense Technical Information Center
Ft. Belvoir, VA
2. Dudley Knox Library
Naval Postgraduate School
Monterey, CA
3. Dr. Alfredo Caro
Lawrence Livermore National Laboratory
Livermore, CA
4. Dr. Magdalena Serrano De Caro
Lawrence Livermore National Laboratory
Livermore, CA
5. Dr. Craig F. Smith
Naval Postgraduate School
Monterey, CA
6. Dr. Xavier K. Maruyama
Naval Postgraduate School
Monterey, CA
7. Dr. James H. Luscombe
Naval Postgraduate School
Monterey, CA
8. Dr. William B. Halsey
Lawrence Livermore National Laboratory
Livermore, CA
9. Dr. Brian D. Wirth
Department of Nuclear Engineering,
University of California - Berkeley
Berkeley, CA